Biophysical Journal
Article

Biophysical Society

# Critical Influence of Cosolutes and Surfaces on the Assembly of Serpin-Derived Amyloid Fibrils

Michael W. Risør,[1,2,*] Dennis W. Juhl,[1,3] Morten Bjerring,[1,3] Joachim Mathiesen,[4] Jan J. Enghild,[1,2] Niels C. Nielsen,[1,3] and Daniel E. Otzen[1,2,*]

[1]Center for Insoluble Protein Structures (inSPIN), Interdisciplinary Nanoscience Center (iNANO), [2]Department of Molecular Biology and Genetics, and [3]Department of Chemistry, Aarhus University, Aarhus, Denmark; and [4]Niels Bohr Institute, University of Copenhagen, Copenhagen, Denmark

ABSTRACT Many proteins and peptides self-associate into highly ordered and structurally similar amyloid cross-$\beta$ aggregates. This fibrillation is critically dependent on properties of the protein and the surrounding environment that alter kinetic and thermodynamic equilibria. Here, we report on dominating surface and solution effects on the fibrillogenic behavior and amyloid assembly of the C-36 peptide, a circulating bioactive peptide from the $\alpha_1$-antitrypsin serine protease inhibitor. C-36 converts from an unstructured peptide to mature amyloid twisted-ribbon fibrils over a few hours when incubated on polystyrene plates under physiological conditions through a pathway dominated by surface-enhanced nucleation. In contrast, in plates with nonbinding surfaces, slow bulk nucleation takes precedence over surface catalysis and leads to fibrillar polymorphism. Fibrillation is strongly ion-sensitive, underlining the interplay between hydrophilic and hydrophobic forces in molecular self-assembly. The addition of exogenous surfaces in the form of silica glass beads and polyanionic heparin molecules potently seeds the amyloid conversion process. In particular, heparin acts as an interacting template that rapidly forces $\beta$-sheet aggregation of C-36 to distinct amyloid species within minutes and leads to a more homogeneous fibril population according to solid-state NMR analysis. Heparin's template effect highlights its role in amyloid seeding and homogeneous self-assembly, which applies both in vitro and in vivo, where glycosaminoglycans are strongly associated with amyloid deposits. Our study illustrates the versatile thermodynamic landscape of amyloid formation and highlights how different experimental conditions direct C-36 into distinct macromolecular structures.

## INTRODUCTION

Amyloid protein deposits are highly ordered fibrillar aggregates with characteristic $\beta$-sheet structures associated with many well-known pathological disorders such as Parkinson's, Alzheimer's, and systemic amyloidosis (1,2). However, coexisting amyloid formation pathways for a single protein and the presence of oligomeric intermediates and polymorphic arrangements complicate our comprehension of the amyloid structure in human disease. The ordered aggregation process is considered to be a nucleated polymerization event involving a fibrillation-competent nucleus (3,4), but external conditions such as ionic strength, cosolutes, and surfaces all modulate the energy landscape of amyloid conversion and ultimately affect both the kinetics of formation and the intra- and interpeptide structural arrangement (5–14). Electrostatic modulation can act on multiple levels by Debye-Hückel ionic screening of peptide charges, "salting-out" Hofmeister effects, and specific ion binding to promote amyloid nucleation, elongation, and conformational conversion from oligomers to amyloid nuclei (15,16). Cosolutes may promote or retard fibrillation through specific binding or through general crowding phenomena (13,17–19). Surfaces represent repetitive molecular arrays that can lower nucleation barriers and stimulate self-assembly through promotion of favorable hydrophobic and hydrophilic interactions (5,20–23). Biological surfaces in the form of lipid membranes and polymeric structural networks such as glycosaminoglycans (GAGs) are particularly relevant for understanding amyloid formation in vivo. The GAGs are constituents of amyloid plaques (24–31) and can accelerate fibril formation and deposition (32–34), dependent on their functional groups (35–37), sulfation degree (38), and polymer chain length (39–41).

*Submitted March 23, 2017, and accepted for publication June 12, 2017.*

*Correspondence: mwrisoer@gmail.com or dao@inano.au.dk

Michael W. Risør's present address is Department of Integrative Structural and Computational Biology, The Scripps Research Institute, La Jolla, CA 92037.

Editor: Elizabeth Rhoades.

http://dx.doi.org/10.1016/j.bpj.2017.06.030

In this study, we provide a comprehensive kinetic description of surface and solution effects on a proteolytically generated amyloid peptide (C-36) from the C-terminal region of the $\alpha$1-antitrypsin ($\alpha_1$AT) serine protease inhibitor. C-36 is intrinsically disordered in solution (42), and has been found in various bodily fluids, in atherosclerotic plaques, and in alveolar fibrillar deposits (43,44). C-36 is bioactive (43) and is also represented in newly detected C-terminal transcripts of the SERPIN1A gene (45). We document how plate surface types (hydrophilic nonbinding surfaces or hydrophobic polystyrene surfaces) and negatively charged surfaces (silica glass beads and heparin polysaccharides) all modulate the amyloid formation of C-36. We demonstrate the surface modulation of microscopic nucleation rate constants by evaluation of global fits to experimental kinetic data of aggregate mass using the framework presented by Knowles and coworkers (46–48). These models have successfully been applied to illustrate the dominating nucleation mechanism of A$\beta$-40 and A$\beta$-42 aggregation (49) and allow us to distinguish between primary and secondary nucleation pathways (details in the Supporting Material). We show that surfaces alter the kinetic terms of fibrillation but also direct C-36 to distinct amyloid morphologies, observed by transmission electron microscopy (TEM) and solid-state NMR. In particular, a negatively charged polyanionic template such as heparin catalyzes a potent template-directed polymerization of C-36 that results in distinct heparin-containing amyloid aggregates. We discuss the effects of solution conditions and polyanionic scaffolds for potentiation and modulation of amyloid formation.

## MATERIALS AND METHODS

### Materials

Unless stated otherwise, all chemicals were from Sigma-Aldrich (St. Louis, MO) and were of analytical grade. All solutions were prepared using deionized water (Milli-Q; Millipore, Billerica, MA). Synthetic C-36 ($NH_2$-SIPPEVKFNKPFVFLMIEQNTKSPLFMGKVVNPTQK-$NH_2$) was made on a solid-phase peptide synthesizer, purified by RP-HPLC and validated with MALDI-MS. Recombinant C-36 (unlabeled and U-[$^{13}$C, $^{15}$N]-labeled was produced as described in Oktaviani et al. (42). Dry peptide powders were solubilized in $H_2O$, the solution was filtered (0.22 $\mu$m), and the peptide concentration was determined using a 2D-Quant kit (GE Healthcare, Little Chalfont, UK). Thioflavin T (ThT) was dissolved to a 10 mM stock solution in 96% ethanol. 9-(2,2-dicyanovinyl) julolidine (DCVJ) was dissolved to a 5 mM stock solution in dimethyl sulfoxide. Heparin sodium salt from bovine intestinal mucosa (H0777; Sigma-Aldrich) was solubilized in $H_2O$ to 10 mg/mL. Silica glass beads ($\phi$ = 1.00–1.18 mm, GP1090; Whitehouse Scientific, Waverton, Cheshire, UK) were washed in 96% ethanol before use. Phosphate-buffered solution (PB) was 20 mM $NaH_2PO_4$/$Na_2HPO_4$, pH 7.42, and phosphate-buffered saline solution (PBS) was 20 mM $NaH_2PO_4$/$Na_2HPO_4$, 150 mM NaCl, pH 7.42. Tris-buffer (TB) was 20 mM Tris, pH 7.42. Tris-buffered-saline (TBS) was 20 mM Tris, 150 mM NaCl, pH 7.42. Ammonium bicarbonate buffer (ABC) was 20 mM $NH_4HCO_3$, pH 7.42. HEPES buffer, 4-(2-hydroxyethyl)-1-piperazineethanesulfonic acid (HEPES), was 20 mM, pH 7.42. MOPS buffer, 3-(N-morpholino)propanesulfonic acid (MOPS), was 20 mM, pH 7.42.

### ThT fibrillation assays

C-36 fibrillation reactions were set up with 40 $\mu$M ThT in a volume of 100 $\mu$L in half-area polystyrene surface plates (PS; Corning microplate #3880, Corning Life Sciences, Tewksbury, MA) and nonbinding surface plates (NBS; Corning microplate #3881) ThT fluorescence was monitored on an Optima FLUOstar plate reader (BMG Labtech, Baden-Württemberg, Germany) with 450 nm excitation and 485 nm emission filters. NBS have a nonionic hydrophilic surface (polyethylene-oxidelike) that minimizes molecular interactions and have been used extensively in several kinetic studies of A$\beta$ "bulk nucleation" and amyloid formation (5,48). PS have a nonpolar surface (owing to the styrene groups) that readily adsorbs protein and which may act as a surface catalyst for nucleation. Fibrillation was carried out at 37°C under quiescent conditions unless otherwise stated. Each condition was assayed in triplicate or quadruplicate and repeated at least twice.

### Concentration-dependent C-36 fibrillation

We measured ThT traces of amyloid formation in PBS at various peptide concentrations, $m_0$ = 2–16 $\mu$M, in PS and NBS plates. Kinetic traces of the fibrillation reactions on each plate were normalized to the maximal fluorescence intensity obtained in the experimental window (28 h for PS, 92 h for NBS) and we assumed sequestration of all monomers into aggregates under all conditions. Polynomial and exponential nucleation growth processes can captured by a global power law scaling behavior, $t_{1/2} \sim {m_0}^{\gamma}$, where $t_{1/2}$ is the time to reach half-completion and $\gamma$ reports on the reaction order of the dominating growth process (46,47) (details in Supporting Material). We plotted $t_{1/2}$ as a function of the peptide concentration on a double-log plot and the linear range was analyzed by the R software package (https://www.r-project.org/) to extract the scaling exponent ($\gamma$) (i.e., the slope in the double-log plot) and SE.

### Evaluation of nucleation pathways by global fitting

The derived scaling exponents for fibrillation in NBS and PS plates ($\gamma_{NBS}$ and $\gamma_{PS}$) were used to calculate the experimental nucleus size ($n$) for primary ($\gamma = -(n_c/2)$) and secondary ($\gamma = -(n_2 + 1/2)$) nucleation-dominated fibrillation based on the mathematical description by Meisl et al. (4), Cohen et al. (46), and Knowles et al. (47). Global fits to average representative ThT curves were carried out with the fibrillation models "nucleation elongation, unseeded" (primary pathway model, PP) and "secondary nucleation dominated, unseeded" (secondary pathway model, SP) in the online program Amylofit (http://www.amylofit.ch.cam.ac.uk/login) (4). The models represent closed analytical solutions to monomer-dependent growth of fibrillar mass as a function of time, $M(t)$. The values of $n_c$ and $n_2$ were used as an empirical restraint for the primary and secondary pathway models, respectively. The model fits were qualitatively evaluated in their ability to represent the experimental curves as a function of the primary and secondary nucleation rate constant terms ($k_n k_+$ and $k_2 k_+$). The rate at which new aggregates are formed ($dP/dt$) in the presence of both primary and secondary nucleation (SP model) is given by

$$\frac{dP}{dt} = k_n[m]^{n_c} + k_2[M]^{n_2},$$

where $[m]$ is the monomer concentration and $[M]$ is the aggregate concentration. If we assume $[m] = m_0$ at the early stages of aggregation, we can calculate the critical aggregate mass fraction ($F_{crit} = M_{crit}/m_0$) at which the primary and secondary nucleation contribute equally to the rate of aggregate formation. The expression of $F_{crit}$ becomes (4)

$$F_{crit} = \frac{M_{crit}}{m_0} \cdot \frac{k_n m_0^{n_c}}{k_2 M_{crit} m_0^{n_2}} = \frac{k_n}{k_2} m_0^{n_c - 1 - n_2}.$$

The value of $F_{crit}$ is used to compare the SP model fits between surfaces for the C-36 data presented herein.

## DCVJ fluorescence

DCVJ was added to a concentration of 20 $\mu$M to probe the presence of prefibrillar and oligomeric intermediate species during C-36 fibrillation (50). DCVJ fluorescence was followed at the same excitation and emission wavelengths used for ThT.

## Heparin-stimulated C-36 fibrillation

We added different heparin amounts to C-36 fibrillation reactions (8 $\mu$M) in PBS in NBS plates and followed the ThT traces. The presence of heparin did not affect the pH of the solution at any of the experimental concentrations. For the purpose of stoichiometric calculations, we specified the polydisperse heparin concentration in disaccharide units ($heparin_{DS}$). We calculated the average mass of the $heparin_{DS}$ unit from compositional data of several heparin fragments (dp10–dp30) published in 2006 in a mass spectrometric characterization of medium-weight heparin (51). Based on the 20 most intense fragments, the $heparin_{DS}$ unit mass was 557 Da with an average sulfate to carboxylate ratio of 2.7 per disaccharide. Accounting for counterion condensation (52) on a 24-disaccharide heparin chain, the sodium counterion fractions (1-$f_{av}$) are $\theta_{Na} = 0.56$ and 0.58 at ionic strengths of 10 and 200 mM (details in the Supporting Material). The average $heaparin_{DS}$ mass with counterions is 605 Da, which was used to determine the $heparin_{DS}$ concentration from the dry weight heparin sodium salt.

## Circular Dichroism spectroscopy

Heparin's effect on the C-36 secondary structure was monitored by wavelength spectra recorded in the far-UV area from 190 to 250 nm on a J-800 spectropolarimeter (Jasco, Oklahoma City, OK) using a quartz cuvette with a 0.1 cm path length and 25 $\mu$M C-36 in 160 $\mu$L PB at 25°C. Time-course profiles at 222 nm for $heparin_{DS}$/peptide ranging from 1.2:1 to 18.5:1 were recorded with a 20 s dead-time that allowed for sample mixing and transfer to the 0.1 cm quartz cuvette. Concurrently, we also measured the ThT trace after a 5:1 $heparin_{DS}$/peptide addition for a PS fibrillation of 25 $\mu$M C-36 in PB in 160 $\mu$L at 25°C. The normalized ThT trace was fitted to a monoexponential function.

## FITC-heparin association with C-36 aggregates

Fluorescein isothiocyanate (FITC)-labeled heparin (50 $\mu$g/mL, 83 $\mu$M) was mixed with different C-36 monomer amounts in 50 $\mu$L PBS. The FITC-heparin disaccharide concentration was calculated by using the $heparin_{DS}$ molecular mass of 605 Da. Reactions were spun down at 15,000*g* after 2 h incubation at 37°C. The fluorescence signal from the residual FITC-heparin in solution was monitored on an Omega FLUOstar plate reader (BMG Labtech) with 485 nm excitation and 520 nm emission filters.

Transmission Electron Microscopy Fibril samples for TEM were spun down, washed once in $H_2O$, and deposited (5 $\mu$L) on a carbon-coated copper grid. The grid was washed once in $H_2O$, stained with 1% uranyl acetate in water, and blotted dry. TEM images were collected using a G2 Tecnai spirit electron microscope (FEI, Hillsboro, OR) operated at 90 KeV with a LaB6 filament. The conditions were identical for all TEM analyses, minimizing any postformation effect on fibril morphology (53).

## Solid-state NMR experiments

Solid-state NMR spectroscopy was carried out on ~5 mg of recombinant U-[$^{13}$C, $^{15}$N]-labeled fibril material produced in the absence or presence of heparin (denoted "N-fibrils" and "H-fibrils", respectively). The N-fibrils were formed by incubation of monomeric C-36 at 50 $\mu$M for five days in PBS under slight agitation. H-fibrils were formed by incubation of monomeric C-36 at 40 $\mu$M in PBS for 8 h at a $heparin_{DS}$/peptide ~16.5:1 (400 $\mu$g/mL heparin). The fibrils were loaded into 4.0 mm MAS rotors and solid-state NMR (ssNMR) spectra were recorded at 1°C at 12 kHz magic angle spinning (MAS) on a 700-MHz spectrometer equipped with a standard triple-resonance 4 mm MAS probe (Bruker BioSpin, Rheinstetten, Germany). $^{13}$C-$^{13}$C correlation spectra were acquired using dipolar assisted rotational resonance (DARR) recoupling (54) with a mixing time of 20 ms. The collected spectra were processed identically (details in the Supporting Material).

# RESULTS

## Differential C-36 fibrillation kinetics on hydrophobic and hydrophilic surfaces

The C-36 peptide forms three $\beta$-strands in its structural context of $\alpha_1$AT but only has a weak $\beta$-strand secondary structural propensity in solution (Fig. 1 *a*). However, a centrally located FVFLM hydrophobic stretch is aggregation prone and ThT fluorescence confirmed potent fibrillation of the C-36 peptide that scaled with neutralization of the peptide's overall charge (Fig. S1 a). The fibrillation resulted in monomer depletion (Fig. S1 b) and displayed a classic sigmoidal shape for pH > 4, which was indicative of a nucleation-dependent polymerization reaction and a hallmark of most amyloid systems (55). We explored surface modulation of C-36 fibrillation by measuring ThT traces of C-36 at monomer concentrations ($m_0$) from 2 to 16 $\mu$M in nonbinding surface plates (NBS) and polystyrene surface plates (PS). Under quiescent conditions, NBS resulted in C-36 fibrillation half-times ranging from 77 h (2 $\mu$M C-36) to 7 h (16 $\mu$M), indicating a relatively slow nucleation process on the nonbinding hydrophilic surface (Fig. 1 *b*). In contrast, PS led to fast C-36 fibrillation with half-times from 7 h (2 $\mu$M) to 2 h (16 $\mu$M) (Fig. 1 *d*). Gel filtration of the peptide before assay start did not diminish the large variability in lag times for low $m_0$ in NBS, suggesting that small aggregates were not the cause of this variation. The ThT plateau level correlated monotonically with $m_0$, although there were small deviations from linearity, particularly at <5 $\mu$M C-36 (Fig. S2).

We employed double logarithmic plots of the fibrillation half-times ($t_{1/2}$) versus $m_0$ to perform a global analysis of the protein aggregation process (4,46,47) (see the Supporting Material for details). The data displayed a global power law scaling behavior ($t_{1/2} \sim m_0^{\gamma}$) expected for nucleation growth processes (Fig. 2 *c*) (46,47). The scaling exponent, $\gamma$, varied with the plate surface type ($\gamma_{PS} = -0.88$, $\gamma_{NBS} = -1.45$) and was reduced with shaking in NBS but not in PS ($\gamma_{PS\text{-}S} = -0.91$, $\gamma_{NBS\text{-}S} = -0.89$). Shaking clearly accelerated fibrillation for both surface types (Fig. 2, *c* and d, *insets*) and for NBS, the concomitant change in $\gamma$ suggested an alteration of the microscopic pathways to a

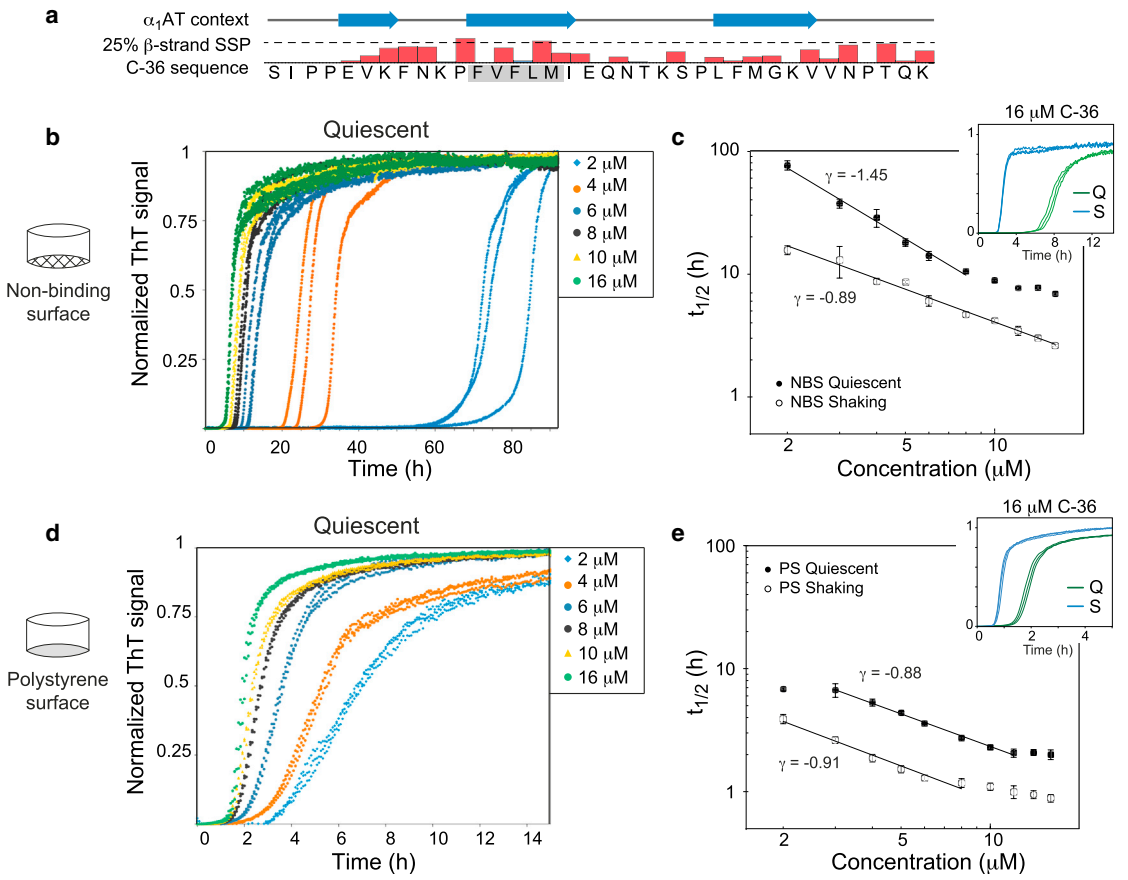


FIGURE 1 Surface type profoundly affects C-36 fibrillation kinetics and alters the balance between primary and secondary nucleation. (*a*) Given here is an overview of the C-36 peptide with indication of the secondary structure in the context of $\alpha_1$AT and the weak $\beta$-strand secondary structural propensity (SSP) in solution determined by liquid-state NMR (adapted from (42)). The aggregation-prone FVFLM is boxed in gray. (*b*) Kinetic traces are displayed in triplicates for C-36 under quiescent conditions carried out in NBS. (*c*) Double logarithmic plots show the time to half-completion ($t_{1/2}$) $\pm$ SD under quiescent or shaking conditions (300 RPM) as a function of C-36 concentration. The scaling relationship for indicated linear fits with SE is $\gamma = -1.45 \pm 0.09$ for quiescent conditions and $\gamma = -0.89 \pm 0.04$ for shaking. (*d*) Kinetic traces are displayed in triplicates for C-36 under quiescent conditions carried out in polystyrene surface plates (PS). (*e*) Double logarithmic plots of the time to half completion ($t_{1/2}$) $\pm$ SD under quiescent or shaking conditions (300 RPM) are given as a function of C-36 concentration. The scaling relationship for indicated linear fits with SE is $\gamma = -0.88 \pm 0.03$ for quiescent conditions and $\gamma = -0.91 \pm 0.03$ for shaking. Insets in (*c*) and (*e*) compare kinetic traces for 16 $\mu$M C-36 under shaking (*S*) and quiescent (*Q*) conditions. To see this figure in color, go online.

more fibril-mass accelerated process. This was also evident from the more steplike curve profile under shaking, all in support of a strong secondary nucleation term enhanced by processes such as filament breakage (48). For PS, the underlying pathways, probed by $\gamma$ and the curve profiles, changed only negligibly with the introduction of shaking. It is important to note that the concentration-dependent fibrillation for NBS and PS under quiescent conditions and for PS under shaking conditions were subject to a small saturation effect for $m_0 > 8$–$10$ $\mu$M, i.e., a flattening of the plot of $t_{1/2}$ versus $m_0$. This positive curvature at higher concentrations indicates a shift in the microscopic pathways as a function of $m_0$, which can relate to saturation of secondary pathways (49). A full treatment of such saturation effects is beyond the scope of the work presented here and we focus primarily on the kinetic data within the linear range of $\gamma$.

## Primary nucleation is enhanced on a polystyrene surface

Global fitting to ThT traces was carried out with the Amylofit analysis platform that contains full analytical solutions to models of amyloid growth (4). Fits of NBS reactions under quiescent conditions ($\gamma_{NBS} = -1.45$) strongly suggested a dominating secondary pathway. The secondary pathway (SP) model, which includes contributions from primary and secondary nucleation, reached satisfactory agreement with experimental results whereas the PP model, which is restricted to primary nucleation alone, failed to do so (Fig. 2, a and b). The SP model did not adequately account for the observed lag-times at higher concentrations that we attribute to the saturation effect and consequent change in $\gamma$ (monomer-dependence). Under shaking conditions with a $\gamma$-value valid for the entire concentration

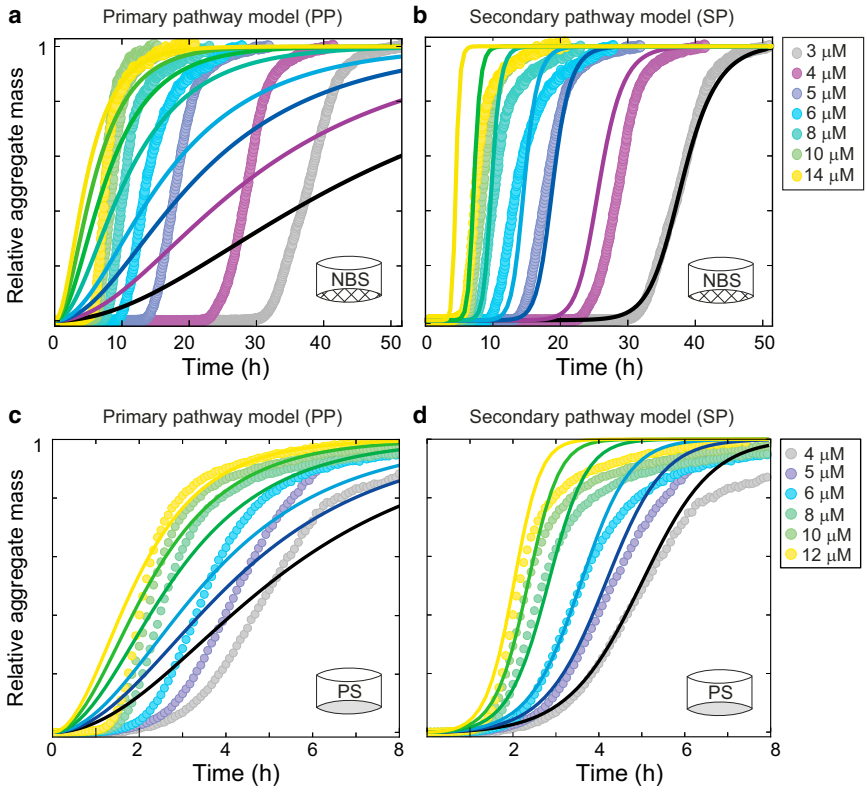


FIGURE 2 Secondary nucleation pathway models describe C-36 fibrillation behavior. Global fits to averaged C-36 time-course profiles were performed with the Amylofit online tool (4). (*a*) The PP model with primary nucleation alone failed to represent the C-36 NBS quiescent data. The nucleus size ($n_c$) was set to 2.9, derived from the $\gamma_{\text{NBS-Q}}$ scaling exponent of $-1.45$ ($\gamma = n_c/2$). (*b*) The SP model with primary and secondary nucleation terms fit the data adequately for lower $m_0$. The nucleus size for secondary nucleation ($n_2$) was set to 1.9 ($\gamma_{\text{NBS-Q}} = (n_2-1)/2 = -1.45$) and $n_c$ was fitted to 1.85. The extracted values for the secondary and primary nucleation contribution were $k_+k_2 = 1.0 \cdot 10^{15}$ and $k_+k_n = 93$, respectively. $F_{\text{crit}}$ at which the two nucleation pathways contributed equally to new aggregate formation was $10^{-8}$ (for $m_0 = 8$ $\mu$M). (*c*) The PP model failed to represent the C-36 PS quiescent data with $n_c = 1.76$, derived from $\gamma_{\text{PS-Q}}$ scaling exponent of $-0.88$. (*d*) The SP model with $n_2$ set to 0.76 and $n_c = 1.425$ (fitted) represented the data up to $t_{1/2}$ adequately. The fit estimates for the secondary and primary nucleation contribution were $k_+k_2 = 2.0 \cdot 10^9$ and $k_+k_n = 2.1 \cdot 10^5$, respectively. $F_{\text{crit}}$ at which the two nucleation pathways contributed equally to new aggregate formation was 0.005 (for $m_0 = 8$ $\mu$M). To see this figure in color, go online.

range, the SP model agreed well with experimental results (Fig. S3 a).

Global fitting to ThT traces under quiescent conditions in PS ($\gamma_{\text{PS}} = -0.88$) failed to produce a satisfactory fit for the PP model alone (Fig. 2 *c*). Early stages of aggregation up to the midpoint of fibrillation were adequately captured by the SP model with a dominant secondary nucleation term (Fig. 2 *d*). However, the SP model fit for PS required a much stronger primary nucleation term compared to the NBS quiescent condition, which was evident from both the rate constants (NBS, $k_2/k_n \sim 10^{13}$; PS, $k_2/k_n \sim 10^4$) and the increase in the fractional aggregate concentration at which new aggregate formation by the secondary nucleation matched the primary nucleation (NBS, $F_{\text{crit}} = 10^{-8}$; PS, $F_{\text{crit}} = 0.005$). The stronger monomer-dependent primary nucleation term in PS plates was consistent with the reduction in lag-times and a reduced exponential shape of the ThT traces compared to the NBS counterparts. Under shaking conditions the SP model reproduced experimental curves for low $m_0$ up to $t_{1/2}$, but also failed to describe the slow decay at later stages of the fibrillation process (Fig. S3 b). We observed a slight improvement of the global fit to PS data with the inclusion of a secondary pathway saturation term (Fig. S4), but a full representation of the curve profile could only be obtained by aborting global fitting and allowing a secondary nucleation rate decrease with concentration (Fig. S4). However, the qualitative evaluation of dominant nucleation mechanisms by global fitting to the simplistic PP and SP models captured surface-induced changes in the microscopic pathways reasonably well and clearly illustrated strong surface effects on aggregation kinetics.

## Polystyrene surface bypasses a pre-ThT hydrophobic species

Amyloid pathways have been shown to involve the formation of oligomeric clusters that can be both on- or off-pathway species, some with distinct structures and cellular toxicity (56–61). To link the distinct differences in kinetics of C-36 fibrillation on NBS or PS to the nature of their primary fibrillation steps and prefibrillar characteristics, we traced C-36 fibrillation with ThT and the DCVJ molecular rotor that reports on hydrophobic prefibrillar oligomers (50,62). For C-36 fibrillation in NBS, a pre-ThT increase in the DCVJ signal was observed (Fig. 3 *a*), suggesting the existence of DCVJ-positive hydrophobic oligomeric clusters preceding the ThT-positive fibrillar species. In contrast, the PS surface produced almost identical time-resolved traces for DCVJ and ThT (Fig. 3 *b*). Bypassing the pre-ThT hydrophobic species on the PS surface was consistent with a strong surface-catalyzed primary nucleation. We interpret the NBS scenario as C-36 nucleation in bulk, which presents low intrinsic primary nucleation and extended lag times in the absence of a stimulatory

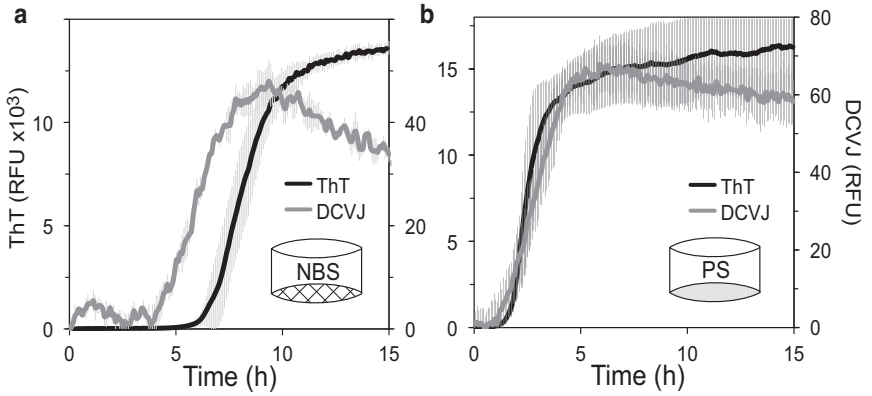


FIGURE 3 The PS surface bypasses a pre-ThT hydrophobic species observed by the DCVJ tracer. ThT and DCVJ fluorescence was measured for 16 $\mu$M C-36 fibrillation reactions in PS and NBS. (*a*) The DCVJ signal (*gray*) preceded the ThT signal (*black*) in NBS plates, potentially probing a pre-ThT oligomeric population. (*b*) The DCVJ and ThT signals displayed highly similar traces in PS plates with no apparent DCVJ increase before the ThT signal. The decrease in the DCVJ signal after reaching its maximal value is interpreted as consolidation of the mature fibrils. Gray error bars indicate the triplicate SD for each point.

hydrophobic surface. We speculate that the formation of hydrophobic oligomeric clusters or the transition of these clusters into more fibrillar species is rate limiting for C-36 amyloid formation under these circumstances.

## Anions potentiate C-36 fibrillation on hydrophobic and hydrophilic surfaces

We used a selection of buffers to evaluate the effect of solvent composition on the C-36 aggregation kinetics in NBS and PS (Fig. 4). The highest aggregation potential was observed in buffers containing phosphate or bicarbonate anions, whereas no ThT-positive fibrillation took place in Tris-buffer or in HEPES and MOPS zwitterionic buffers. These fibrillation-inert buffers did not result in any monomer depletion or other aggregates (data not shown). Monomeric C-36 gave rise to largely identical $^{1}$H-$^{15}$N chemical shift correlations (Fig. S5) in PBS and HEPES. This suggested that the differential aggregation behavior did not relate to any buffer-induced changes in backbone configurations. There was no change in resonance peak shape or relative intensity, suggesting no chemical exchange with other monomer configurations or oligomers (63,64). Rather, potentiation of fibrillation must be associated with promotion of intermolecular contacts by relevant buffer or salt ions via specific ion binding or charge screening (65,66). In evidence of this, C-36 fibrillates in TBS but not TB (which lacks NaCl) and C-36 was also induced to fibrillate in HEPES if sodium chloride (Fig. S6) or phosphate ions were added. C-36 did not aggregate in HEPES buffer even in the presence of the stimulating PS surface or glass beads (data not shown), underlining that transition from a soluble peptide in solution to a highly ordered insoluble $\beta$-sheet aggregate is an environmentally sensitive phase-transition event.

## Glass beads stimulate surface-catalyzed amyloid formation

The strong template-directed surface-catalyzed nucleation of C-36 was further illustrated by fibrillation in NBS in the presence of silica glass beads. The bead surface provided new nucleation terms that entirely overruled the much smaller bulk nucleation rates seen in the absence of beads and caused a profound decrease in the fibrillation lag phase. Increasing the glass surface area (i.e., number of beads) clearly accelerated the fibrillation in a seedlike manner with a semilog relationship between the number of beads and $t_{1/2}$ (Fig. 5 *a*). The presence of one glass bead resulted in a more rounded and less steep ThT trace compared to the control NBS reaction without beads. This suggested a decrease in the aggregate mass-catalyzed secondary growth. The apparent lag time reduction was therefore ascribed to an increased primary nucleation component, similar to the situation on the PS surface. From the ThT traces, we noticed that increasing the number of beads only marginally decreased the growth's infliction point, indicative of a low dependency of primary nucleation on the bead surface area. Instead, the accelerated growth could be explained through global fitting by the secondary nucleation term ($k_+k_2$) that correlated linearly with the number of beads (Fig. 5 *b*). The nucleus sizes resulting in the best fit were $n_c = 2$ and $n_2 = 5$, which reflected the involvement of each pathway in the glass surface-induced effects and was different compared to the situation without beads ($n_c = 1.85$ and $n_2 = 1.9$; Fig. 2 *d*). Based on these findings, we propose that the presence of a glass surface stimulates primary nucleation of C-36 but the largest contribution of the surface is to catalyze seedlike surface-based fibril elongation and secondary nucleation. The DCVJ trace correlated directly with the amyloid mass probed by ThT (Fig. S7), bypassing the preamyloid species detected in the absence of glass beads (Fig. 3 *a*). This is consistent with a surface-nucleated reaction, like the polystyrene surface, where DCVJ and ThT time profiles change in parallel (Fig. 3 *b*).

## Heparin potently modulates C-36 amyloid formation

Heparin is abundant in amyloid deposits and the addition of heparin to C-36 fibrillation reactions caused a

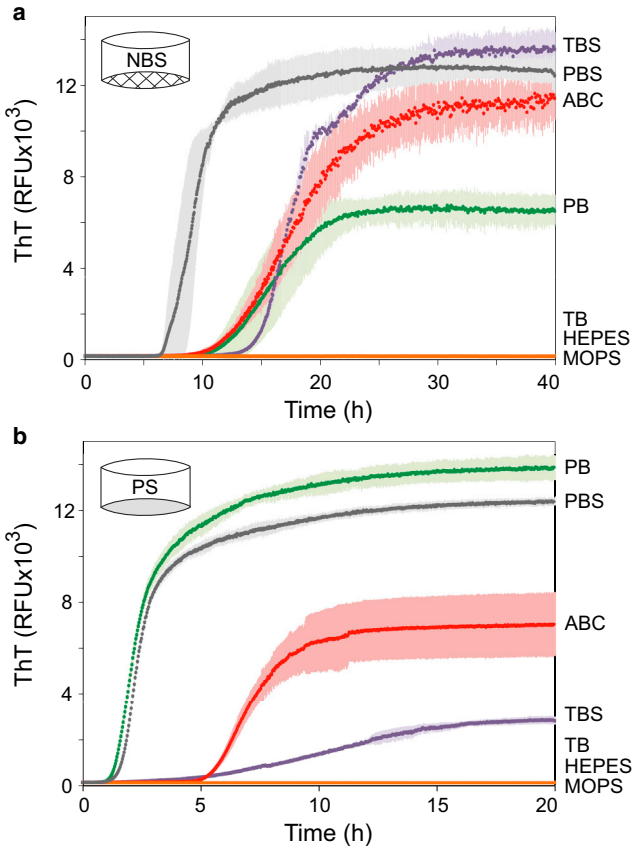


FIGURE 4 Fibrillation is highly affected by the solution composition. C-36 fibrillation kinetics (8 $\mu$M) and ThT endpoint signal showed a large effect of the buffer ion identity and the ionic strength for reactions carried out in NBS (*a*) or PS (*b*). All buffers were prepared to pH 7.42 and had approximate ionic strengths of $I_{PB} = 49$ mM, $I_{PBS} = 200$ mM, $I_{ABC} = 20$ mM, $I_{TB} = 16$ mM, $I_{TBS} = 166$ mM, $I_{HEPES} = 7$ mM, and $I_{MOPS} = 11$ mM. Colored error bars indicate the triplicate SD for each point. TBS is Tris-buffered saline, TB is Tris buffer, PBS is phosphate-buffered saline, PB is phosphate buffer, and ABC is ammonium bicarbonate buffer. See Materials and Methods for exact buffer compositions. To see this figure in color, go online.

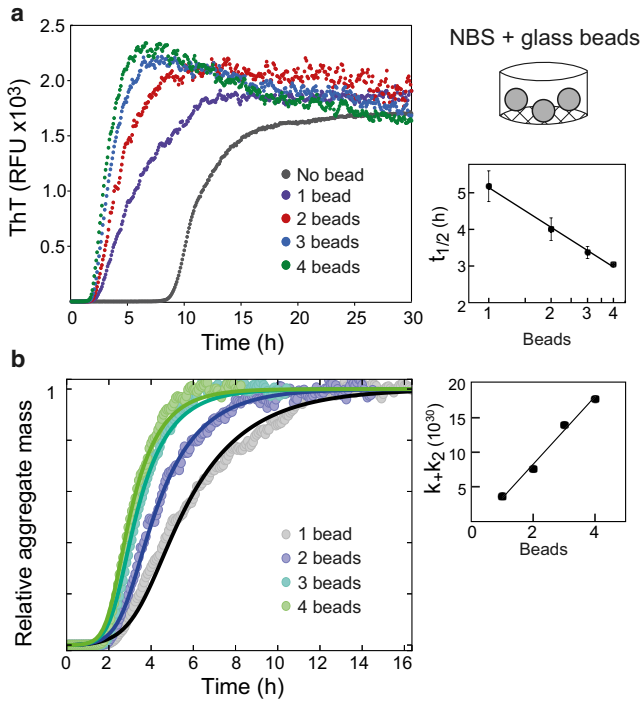


FIGURE 5 An exogenous glass bead surface stimulates nucleation pathways of C-36. (*a*) Shown here are ThT traces of 8 $\mu$M C-36 in PBS with the addition of the indicated number of silica glass beads. A semilog relationship between the number of glass beads and $t_{1/2}$ is observed (*right*). (*b*) Given here are normalized aggregate mass curves using the highest ThT level for each reaction. Global fits to the SP model are displayed with best fit values: $n_c = 2$, $n_2 = 5$, $k_+k_n = 5.7 \cdot 10^7$. The secondary nucleation term, $k_+k_2$, was individually fit to each curve and displayed a linear relationship to the number of glass beads (*right*). $F_{crit}$ at which the two nucleation pathways contributed equally to new aggregate formation in the presence of one glass bead was 0.0038 (for $m_0 = 8$ $\mu$M). To see this figure in color, go online.

potent and concentration-dependent lag phase reduction (Fig. 6 *a*). At heparin disaccharide ($heparin_{DS}$) to peptide ratios > 1:1, the fibrillation acceleration was accompanied by a much smaller fluorescence endpoint signal and the curve profile changed from a sigmoidal shape to a mono-exponential inverted decay. The reaction exhibited a seedlike semilog relationship over a concentration range corresponding to 0.02–1 $heparin_{DS}$ per C-36 peptide (Fig. 6 *b*). Within this range, fitting with the SP model could be achieved by a heparin-dependent contribution to the primary nucleation term (Fig. S8) that supports heparin's role in new aggregate formation. At $heparin_{DS}$/peptide > 2:1, both final ThT levels and $t_{1/2}$ values approached plateau values. The residual monomeric C-36 decreased to almost zero at a high heparin ratio, suggesting that the decrease in ThT endpoint fluorescence was not the result of reduced aggregation (Fig. S9 a). In fact, heparin was able to bind preformed C-36 fibrils (Fig. S9 b) and caused a concentration-dependent ThT fluorescence attenuation (Fig. S9 c). The ThT was not displaced from the fibrillar surface and heparin's effect on the ThT emission could be through shielding of fibril-bound ThT or alteration of ThT's exact binding mode (Fig. S9 d). The aggregation process induced by heparin resulted in a clear concentration-dependent $\beta$-sheet conversion by circular dichroism (CD) spectroscopy (Fig. 6 *c*) and mirrored the ThT signal with a unimolecular association pattern at high $heparin_{DS}$/peptide (Fig. 6 *d*). The association rate was dependent on the amount of heparin (Fig. 6 *d*, *inset*) with a saturation value of ~0.42 $\mu$M/s (Fig. S9 e). The active participation of heparin in the aggregation process was confirmed by the gradual disappearance of FITC-labeled heparin from solution with increasing amounts of C-36 peptide, with an apparent stoichiometry of 1.26 $heparin_{DS}$ per peptide (Fig. 6 *e*). Notably, heparin induced amyloid formation of C-36 also in HEPES and $H_2O$ (where heparin-free C-36 did

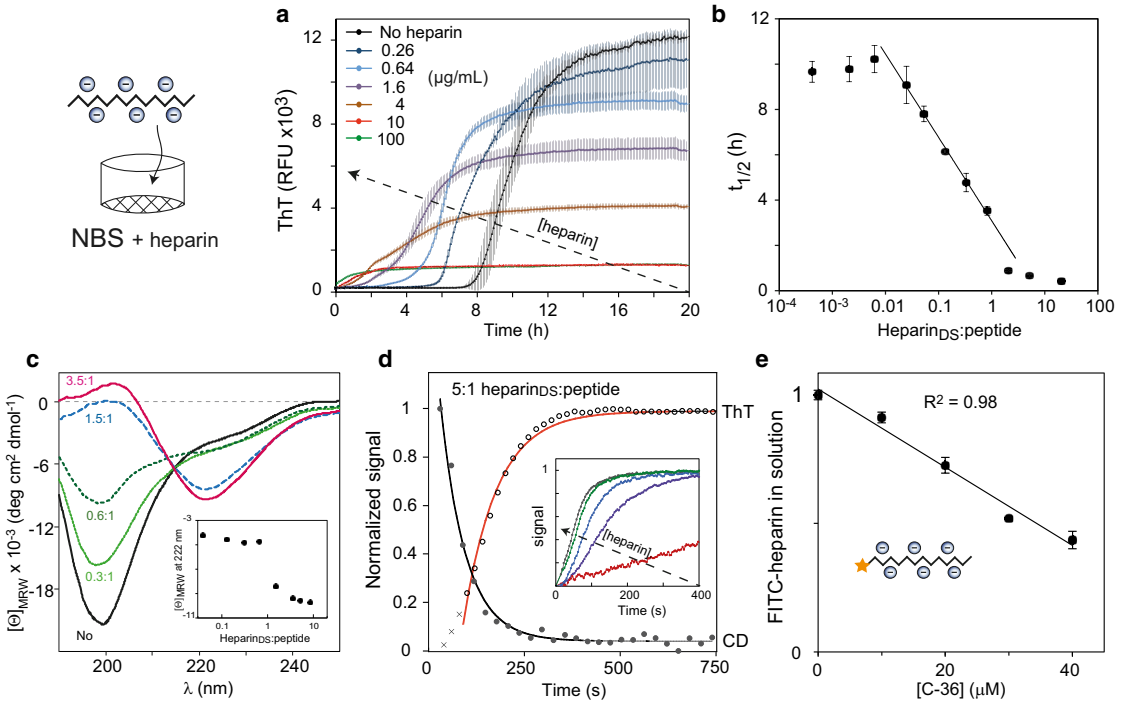


FIGURE 6 Heparin induces rapid C-36 fibrillation and $\beta$-sheet aggregates with lower ThT fluorescence. (*a*) ThT traces of 8 $\mu$M C-36 in PBS show potent alteration of C-36 fibrillation by additions of heparin with lag phase and endpoint ThT reductions. Colored error bars indicate triplicate SD for each point. (*b*) A semilogarithmic plot of the of $t_{1/2}$ as a function of heparin$_{DS}$/peptide reveals a scaling relationship for ratios ranging from 0.02:1 to 1:1, correlating with the heparin-induced ThT fluorescence reduction. (*c*) A clear conversion to $\beta$-sheet is observed by CD (25 $\mu$M peptide) as a function of the heparin$_{DS}$/peptide. Inset shows the mean residue ellipticity change at 222 nm. (*d*) Time-resolved heparin-induced C-36 aggregation is followed by ThT and CD at 222 nm with 25 $\mu$M C-36 and heparin addition to ~5:1 heparin$_{DS}$/peptide. Single exponential fits are shown for each curve with exclusion of the first three data points for the ThT signal (*crosses*). Inset illustrates increasing aggregation speed (normalized 222 nm CD signal) at higher heparin concentrations (29, 58, 115, 231, and 461 $\mu$M). The maximal extrapolated C-36 aggregation rate was 0.42 $\pm$ $\mu$M/s (Fig. S9 *e*). (*e*) FITC-labeled heparin binds C-36 and is removed from solution. FITC-heparin concentration was 50 $\mu$g/mL, corresponding to 83 $\mu$M heparin$_{DS}$. The mean value for heparin$_{DS}$ per C-36 peptide was 1.26 $\pm$ 0.04 (SE) based on the linear regression of two combined independent experiments. To see this figure in color, go online.

not fibrillate), underpinning its highly potent action as an amyloid-inducing biological agent (data not shown).

## Fibril morphology is directed by surface type

We analyzed the morphological species formed by C-36 as a function of surface type to gain a more complete description of surface-guided fibrillation pathways and the underlying energy landscape (53,67–69). TEM imaging of C-36 fibrils formed in PS and NBS revealed clear surface-dependent shifts in fibrillar morphology. The nonbinding surface led to a heterogeneous population of fibrillar species, ranging from abundant small curvilinear fibrils with widths from 5.7 $\pm$ 0.8 nm to large twisted ribbons with widths of 23.4 $\pm$ 3.4 nm (Fig. 7). In contrast, the polystyrene surface-catalyzed fibrils were a homogeneous population of twisted ribbons with average widths of 15 $\pm$ 1 nm and a major periodicity of 56 $\pm$ 3 nm (Fig. 7). These fibril types were also formed in NBS but in much smaller numbers. The morphological appearance of the C-36 fibrils on either surface was reproducible and did not change with $m_0$ or with prolonged incubation or storage. We corroborated the template effect of the surface type by seeding experiments in NBS using either preformed NBS (mixed morphology) or PS seeds (twisted ribbons). In the absence of the polystyrene surface, the PS seeds did not propagate the twisted ribbon morphology but ended up with a mixed morphology characteristic of NBS (Fig. S10 a). Both NBS and PS seeds effectively by-passed primary nucleation, had similar elongation rates, and demonstrated the concentration-dependent scaling behavior predicted by the semilog scaling theory (Fig. S10 b) (47,70).

The addition of external surfaces, glass beads, and heparin, caused clear alterations to the fibrillar morphology that correlated with the aggregation kinetics. The presence of glass beads in NBS resulted in a shift from the mixed NBS morphology to a homogenous twisted ribbon morphology (Fig. 7), which resembled fibrils formed in PS. However, the glass bead ribbon fibrils had a larger twist periodicity (89 $\pm$ 10 nm) and a marginally increased width (16 $\pm$ 1 nm). A closer examination of the PS and glass-induced ribbon fibrils revealed that PS fibrils consisted of three protofibrils, whereas the glass-induced fibrils consisted of four (Fig. S11). Heparin, despite its fast induction of C-36 aggregation, did not result in amorphous structures but also caused

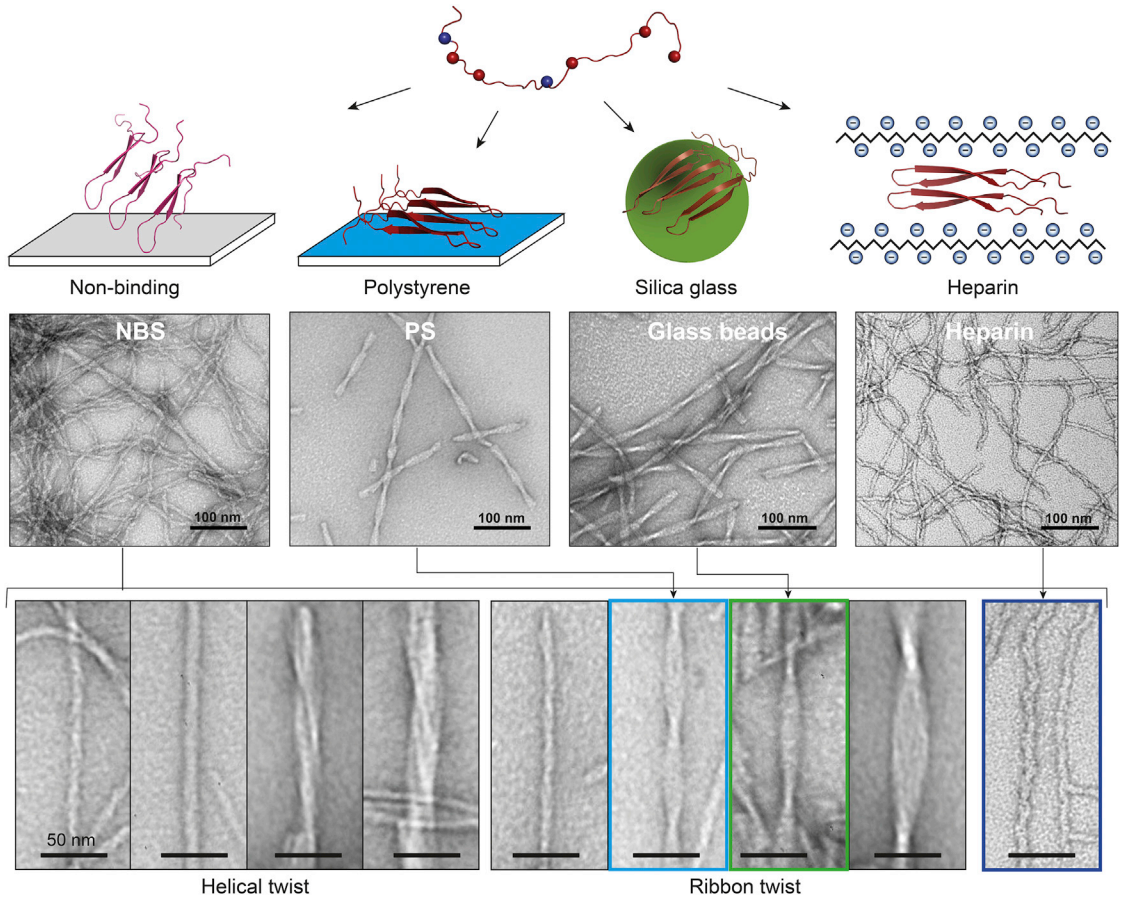


FIGURE 7 Surface-guided fibrillation of C-36 to distinct amyloid arrangements is shown. C-36 is intrinsically disordered in solution and has an overall positive charge. The distribution of charged residues is shown by blue (negative) and red (positive) balls. On nonbinding surfaces, several pathways coexist and lead to a large array of fibrillar structures (*bottom*) with protofibrillar organization into helical and ribbon twist fibrils of various sizes. Polystyrene (*blue*), silica glass (*green*), and heparin (*dark blue*) all bypass a slow primary nucleation to enhance fibrillation rates, likely through a favorable charge compensation by their negative surface. The presence of these stimulating surfaces selectively enhances the formation of distinct fibril morphologies. To see this figure in color, go online.

an ordered amyloid conversion process. The resulting homogenous fibrillar species had a curvilinear appearance and a width of 6.3 ± 1.2 nm ($heparin_{DS}$/peptide > 10:1; Fig. 7). This heparin-induced morphology was caused by heparin's interaction with the C-36 monomer because existing fibrils could not be remodeled by addition of heparin during the course of C-36 fibrillation (Fig. S12). In fact, TEM analysis demonstrated partitioning between ribbon twist or curvilinear fibrils, proportional to the ThT level at the time of heparin addition, which was particularly evident at the $t_{1/2}$ heparin addition ($t$ = 2 h) when the population of the two fibril types was nearly equal (Fig. S12).

## Solid-state NMR probes C-36 fibril diversity and the structural steering by heparin

We prepared recombinant uniformly $^{13}C$,$^{15}N$-labeled C-36 to study fibrillar morphologies in detail by ssNMR. Recombinant C-36 displayed a ThT trace similar to the synthetic version when fibrillated in PS plates (Fig. S13 a). The dominant fibril species was twisted ribbons but a fraction of small curvilinear fibrils was also present (Fig. 8 *a*). Heparin forced the production of homogenous curvilinear fibrils for the recombinant C-36, as observed with the synthetic version (Fig. 8 *a*). Nonheparin fibrils (N-fibrils) and heparin-induced fibrils (H-fibrils) had identical $\beta$-strand signatures by Fourier transform infrared spectroscopy (Fig. S13 b). Distinctly different spectral $^{13}C$-$^{13}C$ correlation signatures were obtained from N- and H-fibrils by DARR ssNMR experiments (Fig. 8 *b*). Firstly, the spectral resolution was improved for H-fibrils compared to N-fibrils, which was evident by the appearance of the two spectra. The improvement for the H-fibrils was likely due to well-defined chemical shifts associated with a more homogeneous structural arrangement. Secondly, unique chemical shifts were observed with H-fibrils in addition to those shared with N-fibrils (Fig. 8, *b* and c). Finally, N-fibrils featured at least three distinct Thr-C$\gamma$ and two Ser-CO resonance crosspeaks, but only two major Thr-C$\gamma$ peaks and one Ser-CO peak were visible in the H-fibrils spectrum. C-36 contains two Thr residues

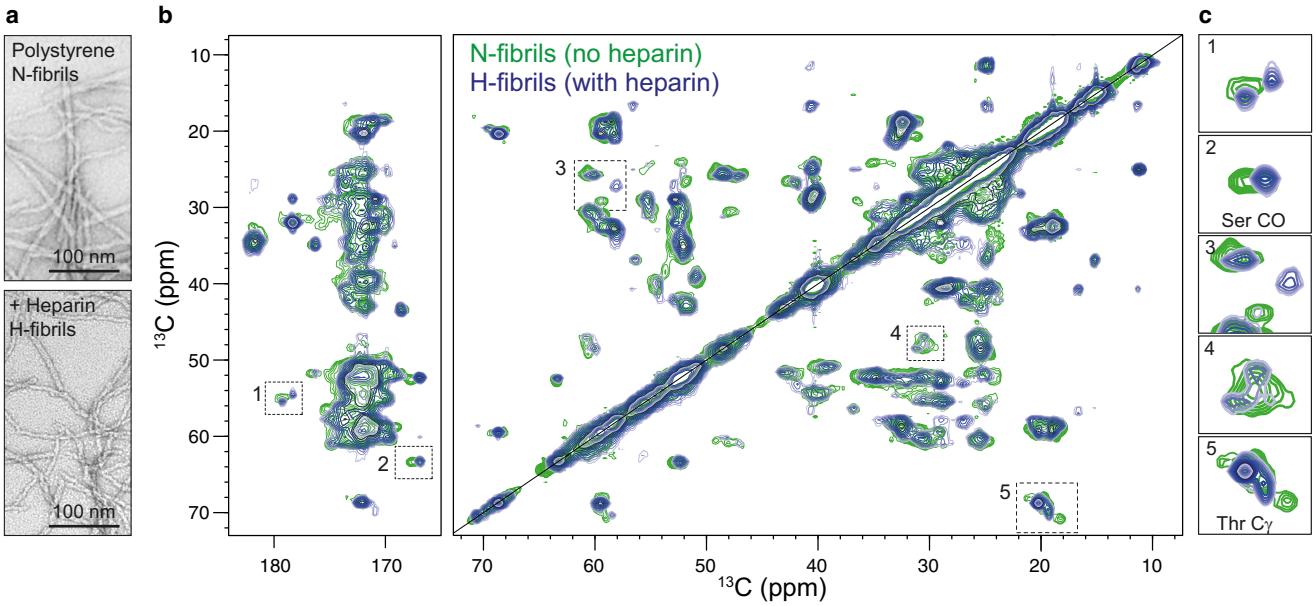


FIGURE 8 Nonheparin and heparin-induced fibrils display atomic level differences by solid-state NMR. (*a*) Given here is the fibril morphology of recombinant C-36 fibrils formed on polystyrene in the absence (N-fibrils) or in the presence (H-fibrils) of heparin. (*b*) Shown here is an overlay of $^{13}$C-$^{13}$C correlation DARR spectra of N-fibrils (*green*) and H-fibrils (*blue*) recorded by MAS ssNMR on a 700 MHz magnet. (*c*) Excerpts from selected chemical shift regions illustrate the clear differences between N- and H-fibrils. To see this figure in color, go online.

(Thr$^{21}$ and Thr$^{34}$) and two Ser residues (Ser$^{1}$ and Ser$^{23}$) (Fig. 1 *a*). The presence of more than two Thr crosspeaks for N-fibrils likely indicates fibril heterogeneity with various structural arrangements represented in the same spectrum. The missing Ser$^{1}$ signal for H-fibrils could be an indication of some flexibility around the N-terminus in these fibrils.

The ssNMR data are consistent with the hypothesis that heparin steers C-36 into a homogeneous fibril structure, of which only a small fraction is present in a fibril population formed without heparin. We did not observe any carbonyl, aromatic, or aliphatic C-36 signals in the mobile phase by INEPT-like J-coupling-based experiments (71,72), indicating a lack of residues with high degree of mobility outside the C-36 fibril arrangement (Fig. S14 a). The presence of crosspeaks from Ser$^{1}$ and Thr$^{34}$ in N-fibrils corroborates a fibrillar arrangement that spans the entire C-36 peptide chain, which is in agreement with a low proteolytic susceptibility of the C-36 fibrils (Fig. S14 b).

## DISCUSSION

### Involvement of surfaces in C-36 amyloid nucleation

Our results suggest that the nucleation of C-36 and its incorporation into distinct amyloid fibrillar structures involves not only intermolecular hydrophobic forces but also surface-based interactions and electrostatic forces that potentiate the hydrophobic clustering and hydrogen bonding leading to a $\beta$-sheet structure. Through our kinetic analysis of C-36 fibrillation, we clearly demonstrated surface-induced enhancement of primary nucleation. The critical aggregate mass fraction, $F_{crit}$, was $10^{-8}$ in NBS and effectively increased to 0.005 in PS and to 0.004 with glass beads. It also increased in the presence of heparin to $5 \cdot 10^{-8}$ for a heparin$_{DS}$/peptide ratio of 0.02, and to 0.001 for a ratio of 2.0. The increase in $F_{crit}$ implies a more dominant role of primary nucleation in the early phases of fibrillation. This more than thousandfold enhancement of primary nucleation compared to bulk nucleation in NBS plates indicates that C-36 has a clear adsorption preference to negatively charged (silica, heparin) and hydrophobic (PS) surfaces versus an NBS at pH 7.4.

The presence of stimulating surfaces (PS, glass beads, and heparin) abrogated a pre-ThT species recognized by DCVJ, suggesting acceleration or by-passing of a rate-limiting step, such as oligomer formation. Surface-induced nucleation likely involves adsorption of the aggregation-prone peptides that may stimulate nucleation through at least three mechanisms. These are: crowding through weak surface-attractive forces resulting in an apparent increase in the local peptide concentration, a situation similar to other crowding phenomena (12,17,73); a surface-induced conformational transition to a $\beta$-prone aggregate state that thermodynamically favors subsequent peptide self-assembly (74,75); and change in the peptide's hydration shell or electrostatic profile that lowers the desolvation barrier and the repulsive Coulombic forces to facilitate nucleation through hydrophobic clustering (5,76–78).

Such hydrophobic clustering has been exemplified in the dynamic adsorption of multiple layers of $\beta$2M on various

nanoparticles that stimulated amyloid formation (79) and in the formation of protein coronas on gold nanoparticles that acted as catalytic seeds (80). For C-36, we found support for a surface-induced conformational transition because PS, silica glass beads, and heparin propagated a homogenous amyloid template whereas the bulk nucleation in NBS did not. The surface enhancement of a particular amyloid arrangement may relate to the exact peptide configuration upon adsorption from which the amyloid seed grows; however, it may also involve an initial condensation followed by structural ordering into a more favorable confirmation (81). Our C-36 results on silica glass beads may be an example of this kind of surface-dependent condensation-ordering event that is less sensitive to the solution concentration of peptide and to the surface area.

## Modulation of amyloid formation by the solution conditions

Protein self-association and adsorption on surfaces is governed by the interplay between electrostatic and van der Waals forces. As a consequence, electrolytes are strong modulators of such interactions through the pH, ionic strength, and specific solute properties. In general, protein aggregation and amyloid formation is affected by salts in several ways. At low ionic strengths ($I < 0.1$ M), salts primarily reduce repulsive electrostatic interactions through Debye-Hückel screening which in turn stimulates aggregation rates, where the slope of $\log(k/k_0)$ versus $\sqrt{I}$ is proportional to the product of the effective charges of the two reacting species (15,82). At intermediate to high ionic strengths, salt ions can promote or delay aggregation by affecting the interfacial hydration layer at surfaces (83,84), empirically ranked in the Hofmeister series (85) (effects reviewed in (86)). Weakly hydrated ions (chaotropes) are readily adsorbed at (protein) surfaces, decrease the interfacial tension, and enhance solubility whereas more strongly hydrated ions (kosmotropes) promote aggregation (87,88). However, many studies of amyloid formation have reported anion specific ion binding effects that scale with the affinity of the ion to an anion-exchange resin, known as the electroselectivity series (66,89,90). In addition, it has also become increasingly clear that weak electrolytes (buffer ions) can play a major role in protein stability, aggregation, and surface adsorption (91–94).

Our broad characterization of C-36 fibrillation in different biological and laboratory buffers demonstrated strong ion-specific effects. The biologically relevant phosphate and bicarbonate systems allowed for C-36 fibrillation to take place without the need for additional salt ($I$ ~20–50 mM), whereas Tris, HEPES, and MOPS did not. Interestingly, buffer ions can specifically modify a protein's overall effective charge, as shown in a case study of lysozyme electrophoretic mobility. The study found that the positively charged protein displayed highest mobility in Tris, whereas it was reduced to ~70% in carbonate and to ~15% in phosphate buffers at pH 7.1 (95). We observed that the maximal C-36 fibrillation rate in PBS was reached around pH 8—well below C-36's isoelectric point of 10.8 (Fig. S1), which supports a potential charge shielding by phosphate. The failure of C-36 to fibrillate in Tris, HEPES, and MOPS could therefore be a consequence of the peptide's charge of $+4e$ at neutral pH that is not efficiently reduced by the solutes to allow self-association. For the zwitterionic HEPES and MOPS buffer ions, a more active role in enhancing the electrostatic repulsion and decreasing attractive van der Waals forces through specific association to positively charged groups is also possible (96). If intrinsic electrostatic repulsions were inhibitory for C-36 self-association, efficient Debye screening using salts would mitigate this effect. Indeed, C-36 fibrillation took place in Tris buffers in the presence of 150 mM NaCl and we observed a clear enhancement of fibrillation in HEPES with increasing ionic strength. HEPES also results in changes of A$\beta$ and hCT fibrillation compared to phosphate-based buffers (91,97); A$\beta$ forms fibrils with delayed kinetics compared to PBS and hCT forms spherical oligomers, supporting that buffer ions have a dramatic effect on peptide self-assembly pathways.

Several studies have described selective ion effects on protein self-association with particular anion binding at the protein surface and anion-mediated acceleration of aggregation (66,98–101). Phosphate and bicarbonate have a kosmotropic nature and also display an ability to specifically bind Lys/Arg-rich sites on proteins and polypeptides (102–105). We speculate that C-36 self-association may be guided by specific anion binding that neutralizes Coulombic electrostatic repulsions between intrinsic lysyl amines in the sequence to facilitate primary nucleation. Site-specific reduction of both intra- and interpeptide repulsions may potentiate the initial contacts through the aggregation-prone pentapeptide-stretch, FVFLM, where $\pi$-stacking of the aromatic rings may play an instrumental role, as seen with other amyloids (106–108).

The surfaces on which fibrillation takes place represent an interface for both solutes and proteins that must also be considered in amyloid studies. We observed great differential solute effects as a function of surface type. On the hydrophobic polystyrene surface, sodium chloride did not accelerate fibrillation in the presence of phosphate, whereas it had a clear catalyzing role on bulk fibrillation (NBS). Conversely, fibrillation in TBS was as potent as in carbonate in bulk, but was markedly reduced on polystyrene and reached a far lower endpoint ThT level. Surfaces have properties related to their chemical nature but their interactions and adsorption properties are also modified by solution conditions through hydration, ion binding, and Hofmeister effects (94). We have shown that the complex solute interplay involves protein-surface as well as protein-protein interactions and is a critical determinant of the amyloidogenic potential and pathway.

## Heparin plays a major role in accelerating amyloid formation

Heparin and heparan sulfate (HS) are negatively charged polyelectrolytes that stimulate amyloidogenesis of several amyloid precursors relevant to human disease such as $\alpha$-synuclein (37), serum amyloid A (109), A$\beta$ (35,110), Tau (111), $\beta$2-macroglobilin (34), IAPP (112), and immunoglobulin light-chain protein (113,114). HS proteoglycans are ubiquitously associated with pathologic amyloid deposits in diseased tissues along with hypersulfated heparin-like forms (115–118). The inhibition of HS biosynthesis and the upregulation of heparanase reduce amyloid load, suggesting that the polyanions play an active role in promoting amyloid deposition in vivo (39,119). Heparin has in recent years been shown to form an active part of amyloid hormone deposits, further highlighting the importance of polyanions in amyloid formation and as biologically active surfaces (120).

The strong acceleration of C-36 fibrillation by heparin and its binding to C-36 with approximately one disaccharide unit per peptide for both monomeric C-36 (1.3:1 binding) and mature fibrils (1:1 binding), demonstrated the active role of heparin in guiding amyloid deposition. Heparin dominated kinetics as well as morphology through direct modulation of the positively charged C-36 monomer, as shown by fluorescence, CD spectroscopy, and TEM. We observed a clear fibrillation rate increase with heparin concentration that saturated at high $\text{heparin}_{\text{DS}}$/peptide. A monomorphic fibril appearance was induced by heparin that did not turn into amorphous aggregates at excess GAGs, as seen in some amyloid systems (40,41,121).

The highly favorable C-36/heparin interaction occurred on a min-to-s timescale and the morphologically distinct heparin aggregates acted as potent seeds for elongation and secondary nucleation at low $\text{heparin}_{\text{DS}}$/peptide. A similar rapid $\beta$-sheet conversion has been observed for amyloid-$\beta$ peptides (41), GAPDH (122), muscle acylphosphatase (123), and calcitonin (124). However, the HS-induced muscle acylphosphatase aggregation also bears a resemblance to C-36 in regard to its fast aggregation at subsaturation followed by a seeded slower aggregation phase (125). Such heterogeneous seeding by HS and heparin is of particular interest because GAG-peptide $\beta$-sheet aggregates may, even in small numbers, drastically affect local amyloid formation in vivo by acting as pathological chaperones that seed various amyloid pathways. In contrast, the complete kinetic and morphological steering by heparin in excess represents sequestration that could, as a general principle, both bypass formation of cytotoxic oligomeric species in amyloid systems and present a less toxic aggregate mass in itself, as demonstrated for apomyoglobin and IAPP (112,121).

Multiple amyloid peptides and proteins interact with heparin based on electrostatic contacts with surface-exposed basic motifs or association to a sufficiently dense positively charged surface (11,121,126,127). In a number of cases, direct contacts have a pH-switch of interaction regulated by protonation of one or several central His residues, such as H36 in Serum amyloid A, H18 in hIAPP, H31 in transthyretin, and H13 in A$\beta$ (11,112,127,128). C-36 lacks His and Arg residues and charge complementarity must be provided by one or several of the five Lys residues (K7, K10, K22, K29, and K36). Heparin interactions are largely driven by entropy through the polyelectrolyte effect, where most of the favorable free energy change comes from the displacement of heparin-bound sodium counterions upon protein binding (129,130). This has been illustrated for the heparin-interacting A$\beta$ (12–18) segment VHHQKL ($+2e$, pH 6.0) and the KWK-CO2 oligopeptide ($+2e$, pH 6.0), both containing consensus BXB motifs and binding one disaccharide unit per peptide (129,131). C-36 (amidated) has a net nominal charge of $+4e$ at a neutral pH and its contact to the heparin disaccharide could be mediated by a favorable entropic interaction through one of the basic motifs, BXXB and $\text{BX}_6\text{B}$. Native heparin consists of $\sim$24 disaccharides, each with a structural mean charge of $-3.7e$, and approximately two monovalent counterions are bound per disaccharide according to counterion condensation theory (see the Supporting Material). Theoretically, C-36 could therefore bind two disaccharides by counterion substitution and our result of $\sim$1.3 is within this limit of an entropy-dominated binding. By ssNMR and TEM, we have shown that heparin steers C-36 into morphologically distinct curvilinear fibrils and remains associated with the fibrillar aggregate. It would be interesting to examine the details of the heparin/C-36 binding, which will require an accurate structural model of the C-36 amyloid fibrils. Such information is accessible through detailed ssNMR studies, as recently demonstrated for heparin's specific interaction with the 3Q morphology of A$\beta$ fibrils (132).

## External factors guide amyloid assembly pathways

Amyloid fibrils represent a thermodynamically favorable state on the protein folding landscape. However, their formation is preceded by a multitude of structural intermediates, ranging from hydrophobic oligomeric assemblies to protofibrils or even amorphous aggregates. An increase in protein concentration can lead to the occurrence of multiple species with less thermodynamic stability, depending on the exact energetics associated with each state (133–135), but extrinsic factors also play a major role in modulating both rate constants and transition energies of various self-assembly pathways. The clear distinction among dominant fibril morphologies on PS, NBS, glass beads, and heparin surfaces demonstrates template-guided morphological steering and strong catalytic enhancements. Because all individual morphological forms were present under bulk nucleation

(NBS) but individually enhanced under strong surface-induced nucleation, including heparin, we ascribe the surface effects to distinct alterations of the thermodynamic landscape. However, the selection of one fibrillation pathway over another required sustained surface stimulation: 1) PS seeds failed to propagate a uniform morphology in the absence of the PS surface and 2) the fraction of H-fibrils in the endpoint fibril population scaled directly to the $\text{heparin}_{DS}$/peptide, despite seeding effects. The strong surface effects clearly reflect alterations of protofibrillar organization, and the spectral properties of N- and H-fibrils by ssNMR support atomic level differences in the $\beta$-strand building block as well.

## CONCLUSIONS

Amyloid formation is involved in numerous human disorders and there is a need to further understand the factors that influence such protein self-assembly processes. In this study, we have shown that both hydrophobic (polystyrene) and negatively charged surfaces (silica glass beads and heparin) lead to accelerated primary nucleation for the positively charged C-36 peptide from $\alpha_1$-antitrypsin. The C-36 peptide contains a serpin-conserved aggregation-prone region, circulates in bodily fluids, and has been found in atherosclerotic plaques. The surface-mediated kinetic enhancement by several orders of magnitude and the bypassing of early oligomeric states led to a select subset of amyloid endpoint structures, which highlights the role of scaffolds for macromolecular assembly. We also demonstrated how the surrounding ionic composition strongly modulated C-36 fibrillation, presumably by increasing or lowering the free energy barrier of nucleation through charge screening and selective ion binding. The charge compensation effect was also evident by the potent stimulation of C-36 fibrillation by polyanionic heparin molecules. Heparin was directly implicated in the formation of amyloid aggregates and guided C-36 to a distinct morphological appearance. Such template-driven conversion is highly relevant for understanding the intricate relationship between biological polyelectrolytes in the context of amyloidosis. Imaging amyloid-GAG deposits in vivo by targeting specific amyloid-associated polyanionic structures has expanded the relevance of this entangled relationship (117,118,136). Therefore, future research into GAG-mediated $\beta$-sheet aggregation and fibrillation should focus on the structural properties of GAG/protein coassemblies. This would not only provide useful information for the modulation of disease amyloid deposition in the complex in vivo environment, but also for understanding the functional roles of GAG-containing secretory granules containing reversible peptide hormone aggregate structures (120,137). Such knowledge is highly relevant to the development of self-regulatory peptide deposits and therapeutic drug functionalization.

## SUPPORTING MATERIAL

Supporting Materials and Methods and fourteen figures are available at http://www.biophysj.org/biophysj/supplemental/S0006-3495(17)30680-X.

## AUTHOR CONTRIBUTIONS

M.W.R., N.C.N., and D.E.O. designed the study. M.W.R. and D.W.J. carried out the experiments. M.B. assisted with ssNMR. J.M. assisted with fibrillation models. M.W.R., D.W.J., D.E.O., N.C.N., and J.J.E. analyzed the results. M.W.R. and D.E.O. wrote the manuscript.

## ACKNOWLEDGMENTS

We are grateful to Erik Holm Nielsen for the chemical synthesis of C-36, Aslan Hüsnu for preliminary AFM screens, and Sharon Preece for manuscript editing and proofreading.

This work was supported by grants from the Danish National Research Foundation (DNRF59), the Program Commission on Strategic Growth Technologies, Innovation Fund Denmark (0603-00439B), and the Carlsberg Foundation.

## SUPPORTING CITATIONS

References (138–145) appear in the Supporting Material.

## REFERENCES

1. Bourdenx, M., N. S. Koulakiotis, …, A. Tsarbopoulos. 2015. Protein aggregation and neurodegeneration in prototypical neurodegenerative diseases: examples of amyloidopathies, tauopathies and synucleinopathies. *Prog. Neurobiol.* 155:171–193.
2. Wechalekar, A. D., J. D. Gillmore, and P. N. Hawkins. 2016. Systemic amyloidosis. *Lancet.* 387:2641–2654.
3. Morris, A. M., M. A. Watzky, and R. G. Finke. 2009. Protein aggregation kinetics, mechanism, and curve-fitting: a review of the literature. *Biochim. Biophys. Acta.* 1794:375–397.
4. Meisl, G., J. B. Kirkegaard, …, T. P. Knowles. 2016. Molecular mechanisms of protein aggregation from global fitting of kinetic models. *Nat. Protoc.* 11:252–272.
5. Vácha, R., S. Linse, and M. Lund. 2014. Surface effects on aggregation kinetics of amyloidogenic peptides. *J. Am. Chem. Soc.* 136:11776–11782.
6. Goers, J., V. N. Uversky, and A. L. Fink. 2003. Polycation-induced oligomerization and accelerated fibrillation of human $\alpha$-synuclein in vitro. *Protein Sci.* 12:702–707.
7. Necula, M., C. N. Chirita, and J. Kuret. 2003. Rapid anionic micelle-mediated $\alpha$-synuclein fibrillization in vitro. *J. Biol. Chem.* 278:46674–46680.
8. Chaudhary, N., and R. Nagaraj. 2011. Self-assembly of short amyloidogenic peptides at the air-water interface. *J. Colloid Interface Sci.* 360:139–147.
9. Moores, B., E. Drolle, …, Z. Leonenko. 2011. Effect of surfaces on amyloid fibril formation. *PLoS One.* 6:e25954.
10. Bonifácio, M. J., Y. Sakaki, and M. J. Saraiva. 1996. 'In vitro' amyloid fibril formation from transthyretin: the influence of ions and the amyloidogenicity of TTR variants. *Biochim. Biophys. Acta.* 1316:35–42.
11. Noborn, F., P. O'Callaghan, …, J. P. Li. 2011. Heparan sulfate/heparin promotes transthyretin fibrillization through selective binding to a basic motif in the protein. *Proc. Natl. Acad. Sci. USA.* 108:5584–5589.

12. Lee, C. F., S. Bird, …, D. J. Vaux. 2012. Combined effects of agitation, macromolecular crowding, and interfaces on amyloidogenesis. *J. Biol. Chem.* 287:38006–38019.
13. Gao, M., K. Estel, …, S. Ebbinghaus. 2015. Modulation of human IAPP fibrillation: cosolutes, crowders and chaperones. *Phys. Chem. Chem. Phys.* 17:8338–8348.
14. Nielsen, L., R. Khurana, …, A. L. Fink. 2001. Effect of environmental factors on the kinetics of insulin fibril formation: elucidation of the molecular mechanism. *Biochemistry.* 40:6036–6046.
15. Buell, A. K., P. Hung, …, T. P. Knowles. 2013. Electrostatic effects in filamentous protein aggregation. *Biophys. J.* 104:1116–1126.
16. Ruzafa, D., F. Conejero-Lara, and B. Morel. 2013. Modulation of the stability of amyloidogenic precursors by anion binding strongly influences the rate of amyloid nucleation. *Phys. Chem. Chem. Phys.* 15:15508–15517.
17. Uversky, V. N., E. M Cooper, …, A. L. Fink. 2002. Accelerated $\alpha$-synuclein fibrillation in crowded milieu. *FEBS Lett.* 515:99–103.
18. Sukenik, S., and D. Harries. 2012. Insights into the disparate action of osmolytes and macromolecular crowders on amyloid formation. *Prion.* 6:26–31.
19. Syme, C. D., R. C. Nadal, …, J. H. Viles. 2004. Copper binding to the amyloid-$\beta$ (A$\beta$) peptide associated with Alzheimer's disease: folding, coordination geometry, pH dependence, stoichiometry, and affinity of A$\beta$-(1–28): insights from a range of complementary spectroscopic techniques. *J. Biol. Chem.* 279:18169–18177.
20. Cabaleiro-Lago, C., F. Quinlan-Pluck, …, S. Linse. 2010. Dual effect of amino modified polystyrene nanoparticles on amyloid $\beta$ protein fibrillation. *ACS Chem. Neurosci.* 1:279–287.
21. Dahse, K., M. Garvey, …, A. Fahr. 2010. DHPC strongly affects the structure and oligomerization propensity of Alzheimer's A$\beta$(1–40) peptide. *J. Mol. Biol.* 403:643–659.
22. Galvagnion, C., A. K. Buell, …, C. M. Dobson. 2015. Lipid vesicles trigger $\alpha$-synuclein aggregation by stimulating primary nucleation. *Nat. Chem. Biol.* 11:229–234.
23. Giehm, L., and D. E. Otzen. 2010. Strategies to increase the reproducibility of protein fibrillization in plate reader assays. *Anal. Biochem.* 400:270–281.
24. Calamai, M., J. R. Kumita, …, C. M. Dobson. 2006. Nature and significance of the interactions between amyloid fibrils and biological polyelectrolytes. *Biochemistry.* 45:12806–12815.
25. Oláh, J., O. Vincze, …, J. Ovádi. 2011. Interactions of pathological hallmark proteins: tubulin polymerization promoting protein/p25, $\beta$-amyloid, and $\alpha$-synuclein. *J. Biol. Chem.* 286:34088–34100.
26. Veerhuis, R., R. S. Boshuizen, and A. Familian. 2005. Amyloid associated proteins in Alzheimer's and prion disease. *Curr. Drug Targets CNS Neurol. Disord.* 4:235–248.
27. Morrison, J. C., N. L. L'Hernault, …, H. A. Quigley. 1989. Ultrastructural location of extracellular matrix components in the optic nerve head. *Arch. Ophthalmol.* 107:123–129.
28. Snow, A. D., R. Kisilevsky, …, S. J. DeArmond. 1989. Sulfated glycosaminoglycans in amyloid plaques of prion diseases. *Acta Neuropathol.* 77:337–342.
29. Snow, A. D., J. P. Willmer, and R. Kisilevsky. 1987. Sulfated glycosaminoglycans in Alzheimer's disease. *Hum. Pathol.* 18:506–510.
30. van Horssen, J., I. Otte-Höller, …, M. M. Verbeek. 2001. Heparan sulfate proteoglycan expression in cerebrovascular amyloid $\beta$ deposits in Alzheimer's disease and hereditary cerebral hemorrhage with amyloidosis (Dutch) brains. *Acta Neuropathol.* 102:604–614.
31. Su, J. H., B. J. Cummings, and C. W. Cotman. 1992. Localization of heparan sulfate glycosaminoglycan and proteoglycan core protein in aged brain and Alzheimer's disease. *Neuroscience.* 51:801–813.
32. Snow, A. D., R. Sekiguchi, …, D. G. Morgan. 1994. An important role of heparan sulfate proteoglycan (Perlecan) in a model system for the deposition and persistence of fibrillar A $\beta$-amyloid in rat brain. *Neuron.* 12:219–234.
33. Ariga, T., T. Miyatake, and R. K. Yu. 2010. Role of proteoglycans and glycosaminoglycans in the pathogenesis of Alzheimer's disease and related disorders: amyloidogenesis and therapeutic strategies—a review. *J. Neurosci. Res.* 88:2303–2315.
34. Borysik, A. J., I. J. Morten, …, E. W. Hewitt. 2007. Specific glycosaminoglycans promote unseeded amyloid formation from $\beta$2-microglobulin under physiological conditions. *Kidney Int.* 72:174–181.
35. Castillo, G. M., W. Lukito, …, A. D. Snow. 1999. The sulfate moieties of glycosaminoglycans are critical for the enhancement of $\beta$-amyloid protein fibril formation. *J. Neurochem.* 72:1681–1687.
36. Castillo, G. M., J. A. Cummings, …, A. D. Snow. 1998. Sulfate content and specific glycosaminoglycan backbone of perlecan are critical for perlecan's enhancement of islet amyloid polypeptide (amylin) fibril formation. *Diabetes.* 47:612–620.
37. Cohlberg, J. A., J. Li, …, A. L. Fink. 2002. Heparin and other glycosaminoglycans stimulate the formation of amyloid fibrils from $\alpha$-synuclein in vitro. *Biochemistry.* 41:1502–1511.
38. Malmos, K. G., and D. E. Otzen. 2013. Glycosaminoglycans and fibrillar polymorphism. *In* Bionanoimaging: Insights into Protein Misfolding and Aggregation. Y. Lyubchenko and V. N. Uversky, editors. Elsevier/Academic Press, New York, pp. 281–290.
39. Li, J. P., M. L. Galvis, …, U. Lindahl. 2005. In vivo fragmentation of heparan sulfate by heparanase overexpression renders mice resistant to amyloid protein A amyloidosis. *Proc. Natl. Acad. Sci. USA.* 102:6473–6477.
40. Nielsen, S. B., P. Yde, …, D. E. Otzen. 2012. Multiple roles of heparin in the aggregation of p25$\alpha$. *J. Mol. Biol.* 421:601–615.
41. McLaurin, J., T. Franklin, X. Zhang, J. Deng, and P. E. Fraser. 1999. Interactions of Alzheimer amyloid-$\beta$ peptides with glycosaminoglycans effects on fibril nucleation and growth. *Eur. J. Biochem.* 266:1101–1110.
42. Oktaviani, N. A., M. W. Risør, …, F. A. Mulder. 2015. Optimized cosolute paramagnetic relaxation enhancement for the rapid NMR analysis of a highly fibrillogenic peptide. *J. Biomol. NMR.* 62:129–142.
43. Subramaniyam, D., P. Glader, …, S. Janciauskiene. 2006. C-36 peptide, a degradation product of $\alpha$1-antitrypsin, modulates human monocyte activation through LPS signaling pathways. *Int. J. Biochem. Cell Biol.* 38:563–575.
44. Dichtl, W., F. Moraga, …, S. Janciauskiene. 2000. The carboxyl-terminal fragment of $\alpha$1-antitrypsin is present in atherosclerotic plaques and regulates inflammatory transcription factors in primary human monocytes. *Mol. Cell Biol. Res. Commun.* 4:50–61.
45. Matamala, N., N. Aggarwal, …, B. Martinez-Delgado. 2017. Identification of novel short C-terminal transcripts of human SERPINA1 gene. *PLoS One.* 12:e0170533.
46. Cohen, S. I., M. Vendruscolo, …, T. J. Knowles. 2013. The kinetics and mechanisms of amyloid formation. *In* Amyloid Fibrils and Prefibrillar Aggregates: Molecular and Biological Properties. D. E. Otzen, editor. Wiley, Weinheim, Germany.
47. Knowles, T. P. J., C. A. Waudby, …, C. M. Dobson. 2009. An analytical solution to the kinetics of breakable filament assembly. *Science.* 326:1533–1537.
48. Cohen, S. I. A., S. Linse, …, T. P. J. Knowles. 2013. Proliferation of amyloid-$\beta$42 aggregates occurs through a secondary nucleation mechanism. *Proc. Natl. Acad. Sci. USA.* 110:9758–9763.
49. Meisl, G., X. Yang, …, T. P. J. Knowles. 2014. Differences in nucleation behavior underlie the contrasting aggregation kinetics of the A$\beta$40 and A$\beta$42 peptides. *Proc. Natl. Acad. Sci. USA.* 111:9384–9389.
50. Lindgren, M., K. Sörgjerd, and P. Hammarström. 2005. Detection and characterization of aggregates, prefibrillar amyloidogenic oligomers, and protofibrils using fluorescence spectroscopy. *Biophys. J.* 88:4200–4212.
51. Henriksen, J., P. Roepstorff, and L. H. Ringborg. 2006. Ion-pairing reversed-phased chromatography/mass spectrometry of heparin. *Carbohydr. Res.* 341:382–387.

52. Manning, G. S. 2008. Approximate solutions to some problems in polyelectrolyte theory involving nonuniform charge distributions. *Macromolecules.* 41:6217–6227.

53. Adamcik, J., and R. Mezzenga. 2011. Adjustable twisting periodic pitch of amyloid fibrils. *Soft Matter.* 7:5437.

54. Takegoshi, K., S. Nakamura, and T. Terao. 2001. $^{13}C$–$^{1}H$ dipolar-assisted rotational resonance in magic-angle spinning NMR. *Chem. Phys. Lett.* 344:631–637.

55. Chiti, F., and C. M. Dobson. 2006. Protein misfolding, functional amyloid, and human disease. *Annu. Rev. Biochem.* 75:333–366.

56. Lorenzen, N., S. B. Nielsen, …, D. E. Otzen. 2014. The role of stable $\alpha$-synuclein oligomers in the molecular events underlying amyloid formation. *J. Am. Chem. Soc.* 136:3859–3868.

57. Chen, S. W., S. Drakulic, …, N. Cremades. 2015. Structural characterization of toxic oligomers that are kinetically trapped during $\alpha$-synuclein fibril formation. *Proc. Natl. Acad. Sci. USA.* 112:E1994–E2003.

58. Stroud, J. C., C. Liu, …, D. Eisenberg. 2012. Toxic fibrillar oligomers of amyloid-$\beta$ have cross-$\beta$ structure. *Proc. Natl. Acad. Sci. USA.* 109:7717–7722.

59. Fändrich, M. 2012. Oligomeric intermediates in amyloid formation: structure determination and mechanisms of toxicity. *J. Mol. Biol.* 421:427–440.

60. Stefani, M. 2012. Structural features and cytotoxicity of amyloid oligomers: implications in Alzheimer's disease and other diseases with amyloid deposits. *Prog. Neurobiol.* 99:226–245.

61. Laganowsky, A., C. Liu, …, D. Eisenberg. 2012. Atomic view of a toxic amyloid small oligomer. *Science.* 335:1228–1231.

62. Paslawski, W., M. Andreasen, …, D. E. Otzen. 2014. High stability and cooperative unfolding of $\alpha$-synuclein oligomers. *Biochemistry.* 53:6252–6263.

63. Yamaguchi, T., K. Matsuzaki, and M. Hoshino. 2011. Transient formation of intermediate conformational states of amyloid-$\beta$ peptide revealed by heteronuclear magnetic resonance spectroscopy. *FEBS Lett.* 585:1097–1102.

64. Fawzi, N. L., J. Ying, …, G. M. Clore. 2010. Kinetics of amyloid $\beta$ monomer-to-oligomer exchange by NMR relaxation. *J. Am. Chem. Soc.* 132:9948–9951.

65. Owczarz, M., A. C. Motta, …, P. Arosio. 2015. A colloidal description of intermolecular interactions driving fibril-fibril aggregation of a model amphiphilic peptide. *Langmuir.* 31:7590–7600.

66. Marek, P. J., V. Patsalo, …, D. P. Raleigh. 2012. Ionic strength effects on amyloid formation by amylin are a complicated interplay among Debye screening, ion selectivity, and Hofmeister effects. *Biochemistry.* 51:8478–8490.

67. Paravastu, A. K., A. T. Petkova, and R. Tycko. 2006. Polymorphic fibril formation by residues 10–40 of the Alzheimer's $\beta$-amyloid peptide. *Biophys. J.* 90:4618–4629.

68. Petkova, A. T., R. D. Leapman, …, R. Tycko. 2005. Self-propagating, molecular-level polymorphism in Alzheimer's $\beta$-amyloid fibrils. *Science.* 307:262–265.

69. Adamcik, J., V. Castelletto, …, R. Mezzenga. 2011. Direct observation of time-resolved polymorphic states in the self-assembly of end-capped heptapeptides. *Angew. Chem. Int. Ed. Engl.* 50:5495–5498.

70. Lorenzen, N., S. I. Cohen, …, D. Otzen. 2012. Role of elongation and secondary pathways in S6 amyloid fibril growth. *Biophys. J.* 102:2167–2175.

71. Hu, K.-N., R. P. McGlinchey, …, R. Tycko. 2011. Segmental polymorphism in a functional amyloid. *Biophys. J.* 101:2242–2250.

72. Kryndushkin, D. S., R. B. Wickner, and R. Tycko. 2011. The core of Ure2p prion fibrils is formed by the N-terminal segment in a parallel cross-$\beta$ structure: evidence from solid-state NMR. *J. Mol. Biol.* 409:263–277.

73. Zhou, Z., J.-B. Fan, …, Y. Liang. 2009. Crowded cell-like environment accelerates the nucleation step of amyloidogenic protein misfolding. *J. Biol. Chem.* 284:30148–30158.

74. Zhu, M., P. O. Souillac, …, A. L. Fink. 2002. Surface-catalyzed amyloid fibril formation. *J. Biol. Chem.* 277:50914–50922.

75. Nault, L., C. Vendrely, …, M. Weidenhaupt. 2013. Peptides that form $\beta$-sheets on hydrophobic surfaces accelerate surface-induced insulin amyloidal aggregation. *FEBS Lett.* 587:1281–1286.

76. Ravikumar, K. M., and W. Hwang. 2011. Role of hydration force in the self-assembly of collagens and amyloid steric zipper filaments. *J. Am. Chem. Soc.* 133:11766–11773.

77. Thirumalai, D., G. Reddy, and J. E. Straub. 2012. Role of water in protein aggregation and amyloid polymorphism. *Acc. Chem. Res.* 45:83–92.

78. Assarsson, A., E. Hellstrand, …, S. Linse. 2014. Charge dependent retardation of amyloid $\beta$ aggregation by hydrophilic proteins. *ACS Chem. Neurosci.* 5:266–274.

79. Linse, S., C. Cabaleiro-Lago, …, K. A. Dawson. 2007. Nucleation of protein fibrillation by nanoparticles. *Proc. Natl. Acad. Sci. USA.* 104:8691–8696.

80. Gladytz, A., B. Abel, and H. J. Risselada. 2016. Gold-induced fibril growth: the mechanism of surface-facilitated amyloid aggregation. *Angew. Chem. Int. Ed. Engl.* 55:11242–11246.

81. Auer, S., A. Trovato, and M. Vendruscolo. 2009. A condensation-ordering mechanism in nanoparticle-catalyzed peptide aggregation. *PLOS Comput. Biol.* 5:e1000458.

82. Kutsch, M., P. Hortmann, …, H. Weingärtner. 2016. Dissecting ion-specific from electrostatic salt effects on amyloid fibrillation: a case study of insulin. *Biointerphases.* 11:019008.

83. Nihonyanagi, S., S. Yamaguchi, and T. Tahara. 2014. Counterion effect on interfacial water at charged interfaces and its relevance to the Hofmeister series. *J. Am. Chem. Soc.* 136:6155–6158.

84. Flores, S. C., J. Kherb, and P. S. Cremer. 2012. Direct and reverse Hofmeister effects on interfacial water structure. *J. Phys. Chem. C.* 116:14408–14413.

85. Kunz, W., J. Henle, and B. W. Ninham. 2004. "Zur lehre von der wirkung der salze" (about the science of the effect of salts): Franz Hofmeister's historical papers. *Curr. Opin. Colloid. Int. Sci.* 9:19–37.

86. Salis, A., and B. W. Ninham. 2014. Models and mechanisms of Hofmeister effects in electrolyte solutions, and colloid and protein systems revisited. *Chem. Soc. Rev.* 43:7358–7377.

87. Bogár, F., F. Bartha, …, A. Dér. 2014. On the Hofmeister effect: fluctuations at the protein-water interface and the surface tension. *J. Phys. Chem. B.* 118:8496–8504.

88. Collins, K. D. 2004. Ions from the Hofmeister series and osmolytes: effects on proteins in solution and in the crystallization process. *Methods.* 34:300–311.

89. Pedersen, J. S., J. M. Flink, …, D. E. Otzen. 2006. Sulfates dramatically stabilize a salt-dependent type of glucagon fibrils. *Biophys. J.* 90:4181–4194.

90. Jain, S., and J. B. Udgaonkar. 2010. Salt-induced modulation of the pathway of amyloid fibril formation by the mouse prion protein. *Biochemistry.* 49:7615–7624.

91. Garvey, M., K. Tepper, …, M. Fändrich. 2011. Phosphate and HEPES buffers potently affect the fibrillation and oligomerization mechanism of Alzheimer's A$\beta$ peptide. *Biochem. Biophys. Res. Commun.* 409:385–388.

92. Zhu, L., X. J. Zhang, …, S. Perrett. 2003. Relationship between stability of folding intermediates and amyloid formation for the yeast prion Ure2p: a quantitative analysis of the effects of pH and buffer system. *J. Mol. Biol.* 328:235–254.

93. Barnett, G. V., V. I. Razinkov, …, C. J. Roberts. 2015. Specific-ion effects on the aggregation mechanisms and protein-protein interactions for anti-streptavidin immunoglobulin $\gamma$-1. *J. Phys. Chem. B.* 119:5793–5804.

94. Cugia, F., S. Sedda, …, A. Salis. 2016. Are specific buffer effects the new frontier of Hofmeister phenomena? Insights from lysozyme adsorption on ordered mesoporous silica. *RSC Advances.* 6:94617–94621.

95. Cugia, F., M. Monduzzi, …, A. Salis. 2013. Interplay of ion specificity, pH and buffers: insights from electrophoretic mobility and pH measurements of lysozyme solutions. *RSC Advances.* 3:5882.

96. Koerner, M. M., L. A. Palacio, …, H. I. Petrache. 2011. Electrodynamics of lipid membrane interactions in the presence of zwitterionic buffers. *Biophys. J.* 101:362–369.

97. Itoh-Watanabe, H., M. Kamihira-Ishijima, …, A. Naito. 2013. Characterization of the spherical intermediates and fibril formation of hCT in HEPES solution using solid-state $^{13}$C-NMR and transmission electron microscopy. *Phys. Chem. Chem. Phys.* 15:16956–16964.

98. Gokarn, Y. R., R. M. Fesinmeyer, …, D. N. Brems. 2011. Effective charge measurements reveal selective and preferential accumulation of anions, but not cations, at the protein surface in dilute salt solutions. *Protein Sci.* 20:580–587.

99. Ronga, L., P. Palladino, …, F. Rossi. 2006. Effect of salts on the structural behavior of hPrP $\alpha$2-helix-derived analogues: the counterion perspective. *J. Pept. Sci.* 12:790–795.

100. Munishkina, L. A., J. Henriques, …, A. L. Fink. 2004. Role of protein-water interactions and electrostatics in $\alpha$-synuclein fibril formation. *Biochemistry.* 43:3289–3300.

101. Poniková, S., A. Antošová, …, E. Sedlák. 2015. Lysozyme stability and amyloid fibrillization dependence on Hofmeister anions in acidic pH. *J. Biol. Inorg. Chem.* 20:921–933.

102. Copley, R. R., and G. J. Barton. 1994. A structural analysis of phosphate and sulphate binding sites in proteins. Estimation of propensities for binding and conservation of phosphate binding sites. *J. Mol. Biol.* 242:321–329.

103. Osheroff, N., D. L. Brautigan, and E. Margoliash. 1980. Mapping of anion binding sites on cytochrome *c* by differential chemical modification of lysine residues. *Proc. Natl. Acad. Sci. USA.* 77:4439–4443.

104. Sträter, N., L. Sun, …, W. N. Lipscomb. 1999. A bicarbonate ion as a general base in the mechanism of peptide hydrolysis by dizinc leucine aminopeptidase. *Proc. Natl. Acad. Sci. USA.* 96:11151–11155.

105. Jin, X. Y., L. Leclercq, …, H. Cottet. 2014. Investigating the influence of phosphate ions on Poly(L-lysine) conformations by Taylor dispersion analysis. *Macromolecules.* 47:5320–5327.

106. Gazit, E. 2002. A possible role for $\pi$-stacking in the self-assembly of amyloid fibrils. *FASEB J.* 16:77–83.

107. Levy, M., N. Garmy, …, J. Fantini. 2006. The minimal amyloid-forming fragment of the islet amyloid polypeptide is a glycolipid-binding domain. *FEBS J.* 273:5724–5735.

108. Marshall, K. E., K. L. Morris, …, L. C. Serpell. 2011. Hydrophobic, aromatic, and electrostatic interactions play a central role in amyloid fibril formation and stability. *Biochemistry.* 50:2061–2071.

109. Aguilera, J. J., F. Zhang, …, W. Colón. 2014. Divergent effect of glycosaminoglycans on the in vitro aggregation of serum amyloid A. *Biochimie.* 104:70–80.

110. McLaurin, J., T. Franklin, …, P. E. Fraser. 1999. Interactions of Alzheimer amyloid-$\beta$ peptides with glycosaminoglycans effects on fibril nucleation and growth. *Eur. J. Biochem.* 266:1101–1110.

111. Goedert, M., R. Jakes, …, R. A. Crowther. 1996. Assembly of microtubule-associated protein tau into Alzheimer-like filaments induced by sulphated glycosaminoglycans. *Nature.* 383:550–553.

112. De Carufel, C. A., P. T. Nguyen, …, S. Bourgault. 2013. New insights into the roles of sulfated glycosaminoglycans in islet amyloid polypeptide amyloidogenesis and cytotoxicity. *Biopolymers.* 100:645–655.

113. Ren, R., Z. Hong, …, V. Trinkaus-Randall. 2010. Role of glycosaminoglycan sulfation in the formation of immunoglobulin light chain amyloid oligomers and fibrils. *J. Biol. Chem.* 285:37672–37682.

114. McLaughlin, R. W., J. K. De Stigter, …, M. Ramirez-Alvarado. 2006. The effects of sodium sulfate, glycosaminoglycans, and Congo Red on the structure, stability, and amyloid formation of an immunoglobulin light-chain protein. *Protein Sci.* 15:1710–1722.

115. Snow, A. D., J. Willmer, and R. Kisilevsky. 1987. Sulfated glycosaminoglycans: a common constituent of all amyloids? *Lab. Invest.* 56:120–123.

116. Zhang, X., and J. P. Li. 2010. Heparan sulfate proteoglycans in amyloidosis. *Prog. Mol. Biol. Transl. Sci.* 93:309–334.

117. Smits, N. C., S. Kurup, …, T. H. van Kuppevelt. 2010. The heparan sulfate motif (GlcNS6S-IdoA2S)3, common in heparin, has a strict topography and is involved in cell behavior and disease. *J. Biol. Chem.* 285:41143–41151.

118. Wall, J. S., T. Richey, …, S. J. Kennel. 2011. In vivo molecular imaging of peripheral amyloidosis using heparin-binding peptides. *Proc. Natl. Acad. Sci. USA.* 108:E586–E594.

119. Kisilevsky, R., W. A. Szarek, …, A. Berkin. 2004. Inhibition of amyloid A amyloidogenesis in vivo and in tissue culture by 4-deoxy analogues of peracetylated 2-acetamido-2-deoxy-$\alpha$- and $\beta$-d-glucose: implications for the treatment of various amyloidoses. *Am. J. Pathol.* 164:2127–2137.

120. Maji, S. K., M. H. Perrin, …, R. Riek. 2009. Functional amyloids as natural storage of peptide hormones in pituitary secretory granules. *Science.* 325:328–332.

121. Vilasi, S., R. Sarcina, …, I. Sirangelo. 2011. Heparin induces harmless fibril formation in amyloidogenic W7FW14F apomyoglobin and amyloid aggregation in wild-type protein in vitro. *PLoS One.* 6:e22076.

122. Torres-Bugeau, C. M., C. L. Ávila, …, R. N. Chehín. 2012. Characterization of heparin-induced glyceraldehyde-3-phosphate dehydrogenase early amyloid-like oligomers and their implication in $\alpha$-synuclein aggregation. *J. Biol. Chem.* 287:2398–2409.

123. Motamedi-Shad, N., E. Monsellier, and F. Chiti. 2009. Amyloid formation by the model protein muscle acylphosphatase is accelerated by heparin and heparan sulphate through a scaffolding-based mechanism. *J. Biochem.* 146:805–814.

124. Malmos, K. G., M. Bjerring, …, D. E. Otzen. 2016. How glycosaminoglycans promote fibrillation of salmon calcitonin. *J. Biol. Chem.* 291:16849–16862.

125. Motamedi-Shad, N., T. Garfagnini, …, F. Chiti. 2012. Rapid oligomer formation of human muscle acylphosphatase induced by heparan sulfate. *Nat. Struct. Mol. Biol.* 19:547–554, S1–S2.

126. Torrent, M., M. V. Nogués, …, E. Boix. 2012. The "CPC clip motif": a conserved structural signature for heparin-binding proteins. *PLoS One.* 7:e42692.

127. McLaurin, J., and P. E. Fraser. 2000. Effect of amino-acid substitutions on Alzheimer's amyloid-$\beta$ peptide-glycosaminoglycan interactions. *Eur. J. Biochem.* 267:6353–6361.

128. Elimova, E., R. Kisilevsky, and J. B. Ancsin. 2009. Heparan sulfate promotes the aggregation of HDL-associated serum amyloid A: evidence for a proamyloidogenic histidine molecular switch. *FASEB J.* 23:3436–3448.

129. Mascotti, D. P., and T. M. Lohman. 1995. Thermodynamics of charged oligopeptide-heparin interactions. *Biochemistry.* 34:2908–2915.

130. Minsky, B. B., T. V. Nguyen, …, P. L. Dubin. 2013. Heparin decamer bridges a growth factor and an oligolysine by different charge-driven interactions. *Biomacromolecules.* 14:4091–4098.

131. Nguyen, K., and D. L. Rabenstein. 2016. Interaction of the heparin-binding consensus sequence of $\beta$-amyloid peptides with heparin and heparin-derived oligosaccharides. *J. Phys. Chem. B.* 120:2187–2197.

132. Stewart, K. L., E. Hughes, …, D. A. Middleton. 2016. Atomic details of the interactions of glycosaminoglycans with amyloid-$\beta$ fibrils. *J. Am. Chem. Soc.* 138:8328–8331.

133. Ricchiuto, P., A. V. Brukhno, and S. Auer. 2012. Protein aggregation: kinetics versus thermodynamics. *J. Phys. Chem. B.* 116:5384–5390.

134. Auer, S., F. Meersman, …, M. Vendruscolo. 2008. A generic mechanism of emergence of amyloid protofilaments from disordered oligomeric aggregates. *PLOS Comput. Biol.* 4:e1000222.

135. Pellarin, R., and A. Caflisch. 2006. Interpreting the aggregation kinetics of amyloid peptides. *J. Mol. Biol.* 360:882–892.

136. Wall, J. S., T. Richey, …, A. Chopra. 2012. (125)I-Labeled single-chain monoclonal antibody, NS4F5, that targets the GlcNS6S-IdoA2S motif of heparan sulfate proteoglycans for the in vivo imaging of peripheral amyloidosis. *Nucl. Med. Biol.* 39:65–75.

137. Dannies, P. S. 2012. Prolactin and growth hormone aggregates in secretory granules: the need to understand the structure of the aggregate. *Endocr. Rev.* 33:254–270.

138. Cohen, S. I. A., M. Vendruscolo, …, T. P. J. Knowles. 2012. From macroscopic measurements to microscopic mechanisms of protein aggregation. *J. Mol. Biol.* 421:160–171.

139. Cohen, S. I. A., M. Vendruscolo, …, T. P. J. Knowles. 2011. Nucleated polymerization with secondary pathways. I. Time evolution of the principal moments. *J. Chem. Phys.* 135:065105.

140. Manning, G. S. 1969. Limiting laws and counterion condensation in polyelectrolyte solutions I. Colligative properties. *J. Chem. Phys.* 51:924–933.

141. Diakun, G. P., H. E. Edwards, …, G. O. Phillips. 1978. The relationship between counterion activity coefficients and the anticoagulant activity of heparin. *Macromolecules.* 11:1110–1114.

142. Rabenstein, D. L., J. M. Robert, and J. Peng. 1995. Multinuclear magnetic resonance studies of the interaction of inorganic cations with heparin. *Carbohydr. Res.* 278:239–256.

143. Beirne, J., H. Truchan, and L. Rao. 2011. Development and qualification of a size exclusion chromatography coupled with multiangle light scattering method for molecular weight determination of unfractionated heparin. *Anal. Bioanal. Chem.* 399:717–725.

144. Fung, B. M., A. K. Khitrin, and K. Ermolaev. 2000. An improved broadband decoupling sequence for liquid crystals and solids. *J. Magn. Reson.* 142:97–101.

145. Zandomeneghi, G., M. R. Krebs, …, M. Fändrich. 2004. FTIR reveals structural differences between native $\beta$-sheet proteins and amyloid fibrils. *Protein Sci.* 13:3314–3321.

**Biophysical Journal, Volume *113***

## Supplemental Information

# Critical Influence of Cosolutes and Surfaces on the Assembly of Serpin-Derived Amyloid Fibrils

**Michael W. Risør, Dennis W. Juhl, Morten Bjerring, Joachim Mathiesen, Jan J. Enghild, Niels C. Nielsen, and Daniel E. Otzen**

# SUPPORTING MATERIAL

## Critical influence of co-solutes and surfaces on the assembly of serpin-derived amyloid fibrils

M.W. Risør, D.W. Juhl, M. Bjerring, J. Mathiesen, J.J. Enghild, N.C. Nielsen and D.E. Otzen

## TABLE OF CONTENTS

# SUPPORTING MATERIALS AND METHODS

## THEORETICAL SECTION

### *Time-evolution of a fibrillating system*

The time evolution of a fibrillating system can be described as a combination of the rate constants for the primary ($k_n$) and secondary ($k_2$) nucleation pathways, and fibril elongation ($k_+$). Primary nucleation pathways display strong monomer dependence and result in polynomial growth of aggregate mass, $M(t) \sim \lambda^2 t^2$ with $\lambda = \sqrt{2k_+k_n m^{n_c}}$ where $M$ is the aggregate mass, $m$ is the monomer concentration, and $n_c$ is the nucleus size. Secondary pathways represent processes that depend on the total aggregate mass such as nucleation sites on the fibrillar surface or fibril fragmentation, and result in exponential growth with a clear lag-phase owing to the autocatalytic term $M(t) \sim \exp(\kappa t)$ with $\kappa = \sqrt{2k_+k_2 m^{n_2+1}}$ (1-3). The monomer dependence of the fibrillation reaction is reflected by a power-law relationship, $t_{1/2} = m_0^{\gamma}$, where $t_{1/2}$ represents the time to reach half-maximal aggregate mass (could also be lag-time, $t_{lag}$) and $m_0$ is the initial monomer concentration. The scaling exponent, $\gamma$, conveniently captures the effects of either $\lambda$ or $\kappa$. As a result, the scaling exponent can take form of either $\frac{-n_c}{2}$ for primary nucleation (reflecting $\lambda$) or $\frac{-(n_c-1)}{2}$ for secondary nucleation (reflecting $\kappa$). If monomer-independent processes such as fibril fragmentation dominate, the exponent can display weaker monomer dependence approximating –½ which represents the specialized case where $n_2 = 0$ (1-3). Importantly, primary nucleation can be catalyzed by surfaces (heterogeneous nucleation) which lower the energy barrier for the self-association process. Secondary pathways involve both monomer-dependent and -independent terms, in which secondary nucleation at the fibrillar surface represents the former, and filament fragmentation represents the latter. See Knowles and coworkers for additional details about the microscopic rate constants and the closed analytical solutions used to model amyloid growth phenomena (1, 2, 4, 5).

### *Heparin charge fraction calculation using counterion condensation theory*

Heparin is a polyanion subject to counterion condensation in which a layer of condensed and mobile counterions results in a constant critical net charge density. The structural charge is reduced to a mean effective charge fraction, $f_{av}$, per polyion charge, which is the average of the charge fraction, f(s), for each charge site, P, along the polymer of length L. For end segments,

where the charge's distance from the end is smaller than the Debye screening length, f(s) is expressed as (6): $f(s) = \frac{1}{2z\xi}\left(1 - \frac{\ln \kappa b}{\ln s/b}\right)$, where z is the charge per site, $\xi$ is the charge density parameter, $\kappa$ is the inverse of the Debye screening length, b is the axial spacing between neighboring charged groups, b = (P-1)/L, and s is the distance from the end. For the interior of the polymer, s > 1/κ , f(s) is a constant charge fraction expressed as (7): f(s)= 1/(zξ). A convenient formula for the Debye screening length as a function of ionic strength, *I,* is 1/κ = $0.305I^{-1/2}$, which is valid in water at room temperature with a Bjerrum length ($l_b$) of 0.71 (6). The charge density is expressed as ξ = $l_b$/b. We calculated $f_{av}$ for native heparin assuming an average of 24 disaccharides per heparin chain (89 structural charges). With a disaccharide length of 1.02 nm (8), b = 0.28 nm, and ξ = 2.55. For an ionic strength of 10 mM, 1/κ = 3.05 nm, and $f_{av}$ = 0.44 with the interior polymer f(s) defined > 12 charge sites from the end. For an ionic strength of 200 mM (PBS), 1/κ = 0.68 nm, and $f_{av}$ = 0.42 with the interior polymer f(s) defined > 3 charge sites from the end. The resulting sodium counterion fractions (1-$f_{av}$) are $\theta_{Na}$ = 0.56 and 0.58 at I = 10 and 200 mM, respectively, which agree with experimentally determined values (9). With a sodium mass contribution of 48 Da per disaccharide (I = 10 mM) and a heparin disaccharide average unit mass of 591 Da (see main text), we get the average $heparin_{DS}$ with counterions = 605 Da. We used this mass for calculations of the heparin concentration. The molecular weight of 24 $heparin_{DS}$ units with counterions is 14.5 kDa which agrees with the $M_n$ = 14.1 kDa found in the extensive MALS analysis of unfractionated heparin by Beirne et al. (10).

## EXPERIMENTAL SECTION

### *pH-dependent fibrillation of C-36*

Fibrillation reactions of 8 µM C-36 in PBS adjusted to pH 4.0, 5.0, 6.0, 7.0, 8.0, and 9.0 were carried out in half-area 96-well PS microplates with 40 µM ThT. The resulting ThT traces were normalized to the maximally obtained fluorescence value within the experimental window of 30h.

### *Quantification of residual C-36 monomer*

Fibrillation reactions of 8 µM C-36 in PBS, pH 7.42, were prepared in half-area 96-well PS microplates with 40 µM ThT. The supernatant was pooled from three reactions for eight different time points during fibrillation. Gel filtration analysis was performed on 200 µL of the supernatant using a Superdex Peptide column equilibrated in PBS. The residual monomer amount was quantified by the integrals of the eluted monomeric C-36 peak.

### *Preparation of ThT traces for global fitting*

The global fitting to models of primary and secondary nucleation was carried out using averaged ThT curves. These curves were generated by shifting each experimental ThT trace to the average $t_{1/2}$ of the triplicate, followed by averaging of each shifted triplicate. This ensured a correct representation of the curve profile which otherwise would have been skewed for some concentration points due to the lag-time variations within the triplicates.

### *Seeded C-36 fibrillation*

C-36 (16 µM) was fibrillated in PS and NBS plates under quiescent conditions for two days to generate PS and NBS fibrils for seeds. ThT levels were monitored to validate the fibrillation reaction was complete. The seed material was prepared by extracting fibrils from the plates by thorough pipetting, followed by bath sonication for 10 min. Before sonication, a small fraction of the NBS and PS fibrillar seed material was analyzed by transmission electron microscopy (TEM) to validate the fibrillar seed morphology. Seeded reactions were prepared with 8 µM C-36 using seed concentrations ranging from 0-16%. Each condition was conducted in triplicate and the assay was repeated twice to verify consistent results. Fibril elongation rates for both seed types were extracted during the initial phase of the reactions (< 25 min).

### *Heparin addition to C-36 during fibrillation*

Multiple C-36 fibrillation reactions (10 µM, 150 µL) were conducted in PS plates in PBS and the

ThT signals were monitored. Heparin was added (50 µg/mL, 8:1 $heparin_{DS}$:peptide) to reactions at seven different time points when ThT levels had reached ~ 0, 10, 25, 50, 75, 82, 93, and 96% of the final endpoint value. The reactions were allowed to proceed for 24h. Heparin additions were done in triplicate at every time point and the endpoint fibrils were harvested, redissolved in $H_2O$, and analyzed by TEM. Because ribbon twist fibrils dominated the PS surface and heparin induced curvilinear fibrils, we could visualize the contribution from each fibrillation pathway by TEM.

***Heparin effect on ThT fluorescence from pre-formed C-36 fibrils***

C-36 was fibrillated in NBS plates (8 µM reactions) in the presence of ThT (40 µM) for 48h. The effect of heparin on the endpoint ThT fluorescence was assessed by adding heparin (10 µg/mL to 200 µg/mL) to the C-36 reactions. The endpoint ThT fluorescence reduction was assessed after 50 min of equilibration and plotted as a function of heparin concentration.

***FITC-heparin association with C-36 fibrils***

We mixed 35 µM or 5 µM fluorescein isothiocyanate (FITC)-labeled heparin with pre-formed C-36 fibrils. Different FITC-heparin solutions were used to sample both high and low $heparin_{DS}$:peptide ratios using the same fibril stock. C-36 fibrils were formed by three days incubation in PBS at 50 µM peptide concentration. We confirmed that the FITC-heparin signal in the supernatant with C-36 fibrils was reduced compared to the supernatant without C-36 fibrils. The ratio of bound heparin (in units of disaccharide, $heparin_{DS}$) per C-36 monomer was calculated based on a FITC-heparin standard curve. The FITC-heparin disaccharide concentrations were calculated by using the $heparin_{DS}$ MW of 605 Da and did not account for the FITC-moiety's mass contribution. Reactions were mixed in a total volume of 50 µL, incubated for 2h at 37 °C, and then spun down at 15,000 g. The supernatant was transferred to a 96-well half-area plate and diluted twice. The fluorescence signal from the residual FITC-heparin in solution was monitored on an Omega Fluostar plate reader with 485 nm excitation and 520 nm emission filters.

***Fourier Transform Infrared Spectroscopy (FT-IR)***

FT-IR spectra were measured on monomer and fibrillar C-36 material using a Tensor27 FTIR spectrometer (Bruker) equipped with attenuated total reflection accessory with a continuous flow of $N_2$ gas. The material was spotted into the target plate and dried under nitrogen flow before recording the spectra, and 128 scans were averaged for each spectrum. After compensation for

atmospheric contributions, the absorbance was depicted relative to the largest peak intensity and peak positions were identified from second derivative analysis.

***Liquid-state NMR experimental details***

Samples for liquid-state NMR were prepared at 200 μM C-36 with 20 mM $Na_2HPO_4$, pH 7.0 (PB buffer), and 20 mM HEPES, pH 7.0 (HEPES buffer). We added 8% $D_2O$ (v/v) for the lock and 50 μM DSS for referencing. The inert paramagnetic agent, FeDO3A, was added to both samples to reach a final concentration of 10 mM for rapid acquisition through paramagnetic relaxation enhancement, as previously reported (11). The samples were mixed at 4 °C to prevent premature aggregation. All experiments were carried out at 5 °C using a Bruker 500 MHz spectrometer. We conducted $^{1}H$-$^{15}N$-HSQC experiments with a recycle delay of 100 ms, 2048 ($^{1}H$) x 256 ($^{15}N$) complex points, 32 ppm spectral width ($^{15}N$), and a carrier at 117 ppm. Experiment time was less than 5 min for each individual spectrum, excluding the effect of aggregate formation on the spectral quality and dispersion.

***Solid-state NMR experimental details***

Uniformly ($^{15}N$-$^{13}C$)-labeled non-heparin fibrils (N-fibrils) and heparin-fibrils (H-fibrils) were formed in standard polypropylene tubes (15 mL and 50 mL) and resulted in complete monomer depletion and morphological appearances comparable to recombinant C-36 fibrils formed in PS plates with and without heparin. The fibrils were spun down at 50.000 g and resuspended in 10 mM PB buffer (N-fibrils) or 10 mM PB buffer with 100 μg/mL heparin (H-fibrils). We recorded ssNMR spectra at 1 °C at 12 kHz magic angle spinning on a 700 MHz Bruker spectrometer. To probe potential mobile regions of N-fibrils, we acquired 1D CP and refocused INEPT with $^{1}H$ decoupling with 4096 direct points, 512 scans, and equal receiver gains for comparison. This strategy has successfully revealed mobile regions of other fibril systems (12, 13). The $^{13}C$-$^{13}C$ correlation DARR experiments for N- and H-fibrils were each carried out with 4K x 256 complex points, 80 scans per increment, 200 ppm indirect spectral width, a carrier frequency at 100 ppm, and 80 kHz Spinal-64 $^{1}H$ decoupling (14). Processing was done with 4K x 256 points, an EM window function with LB set to 50 Hz (direct) and 30 Hz (indirect), the GB set to 0 (direct) and 0.1 (indirect), and SSB set to 2 for both dimensions. We referenced the spectra to TMS using an external sample of adamantane with the $CH_2$ signal at 38.48 ppm.

***Proteolytic susceptibility of fibrils***

C-36 fibril and monomer samples (~2 µg) were incubated for 2h with thermolysin or trypsin at the indicated stoichiometry to address the degree of resistance towards proteolysis in the amyloid fibrils. We evaluated the products were using tricine gels for optimal separation of low molecular weight products.

## SUPPORTING FIGURES S1-S14

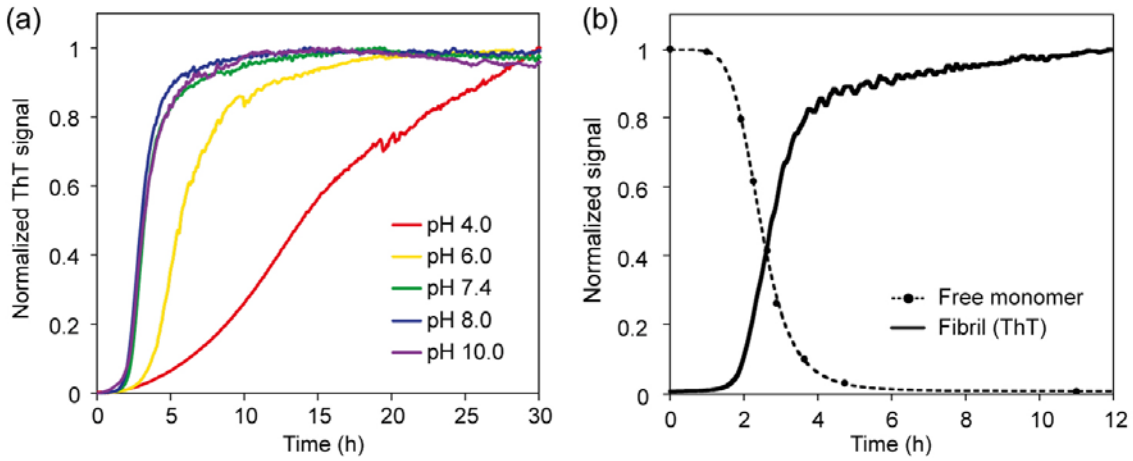


***FIGURE S1 C-36 fibrillates at physiological pH and leads to monomer depletion***
(a) Normalized traces of C-36 fibril formation (8 µM) by ThT fluorescence at the indicated pH values in PBS using PS plates. (b) Fibrillation by ThT fluorescence (8 µM C-36 in PBS, pH 7.42) leads to monomer depletion. The free monomer concentration was measured by gel filtration.

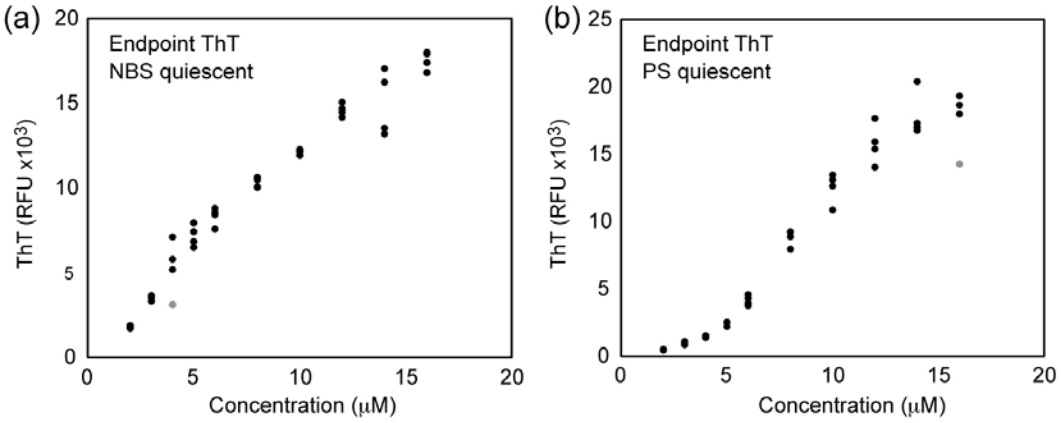


***FIGURE S2 Correlation of the endpoint ThT with the C-36 concentration***
Fibrillation was conducted on NBS and PS plates for various C-36 concentrations as shown in Fig. 1 (main text). (a) For NBS plates, the endpoint ThT level (after 92 h) correlated relatively well with the C-36 concentration. (b) For PS plates, lower peptide concentrations had a slightly smaller relative fluorescence compared to higher concentrations. This could be caused by a critical C-36 concentration below which monomers did not continue to associate with the fibril mass. For the kinetic treatments, we assumed that all peptide was full converted to aggregate mass at the ThT plateau level.

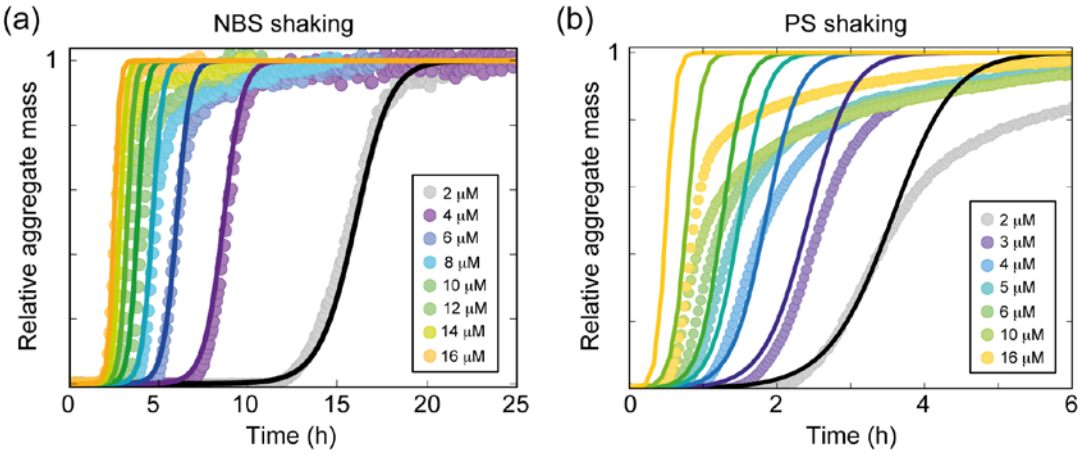


***FIGURE S3 Global SP model fits to aggregate mass under shaking conditions***
(a) Global fit to NBS shaking ThT traces using the SP-model with both primary and secondary nucleation. The nucleus size for secondary nucleation ($n_2$) was set to 0.78, derived from the $\gamma_{NBS-S}$ scaling exponent of -0.88 that was valid for the entire concentration range. The nucleus size for primary nucleation ($n_c$) was set to 1.85, similar to the SP model for the NBS quiescent data. The extracted values for the secondary and primary nucleation contribution were $k_+k_2 = 6.5 \cdot 10^9$ and $k_+k_n = 7 \cdot 10^3$. The NBS shaking ThT traces displayed a steep ThT signal increase after the initial lag phase and rapidly reached plateau values compared to fibrillation under quiescent conditions. This "sawtooth" time profile can arise from a multi-exponential monomer-independent process such as filament breakage (1, 3). (b) Global fit to PS shaking ThT traces using the SP model with $n_2$ set to 0.82 (from a $\gamma_{PS-S}$ scaling exponent of -0.91) and $n_c$ fitted to 2.1. The extracted values for the secondary and primary nucleation contribution were $k_+k_2 = 6 \cdot 10^{10}$ and $k_+k_n = 1.5 \cdot 10^9$. The model only partially represented the data at low concentrations (2-6 μM) and could not explain the slower growth of aggregate mass after $t_{1/2}$. Introduction of shaking clearly accelerated the ordered amyloid conversion but because the nature of the dominating nucleation term was unaltered ($\gamma_{PS-Q} \sim \gamma_{PS-}$), the PS surface may prevent fragmentation from becoming a strong secondary pathway.

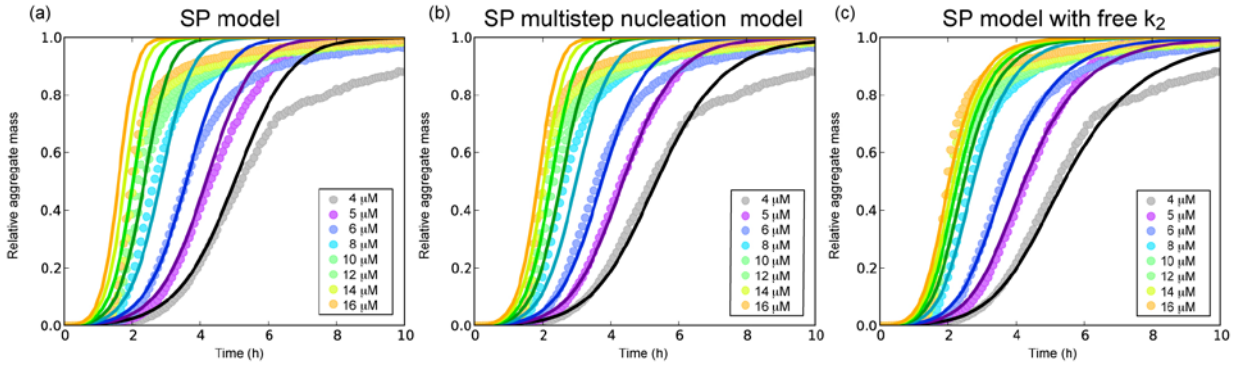


***FIGURE S4 Alternative SP model fits to C-36 PS quiescent data***

(a) The simple SP model fit. New aggregates (P) are generated according to (5): $\frac{dP}{dt} = k_n[m]^{n_c} + k_2[m]^{n_c}[M]$ with $n_c$ = 1.43, $n_c$ = 0.76, $k_+k_n$= $2.0 \cdot 10^9$, and $k_+k_n$ = $2.1 \cdot 10^5$. (b) The secondary pathway model with multistep nucleation model fit. In brief, this model incorporates a saturation term, $K_m$, which scales the new aggregate formation from secondary nucleation with the monomer concentration in a Michaelis-Menten-like fashion (15): $\frac{dP}{dt} = k_n[m]^{n_c} + k_2 \frac{[m]^{n_c}}{1+ [m]^{n_c}/K_m}[M]$. The model was globally fitted to the experimental traces with $n_c$=1.44, $n_2$=2, $k_+k_n$,= $2.0 \cdot 10^5$, $k_+k_2$ = $2.0 \cdot 10^{16}$, and $K_m$ = $1.7 \cdot 10^{-11}$. $K_m$ is given in units of $conc^{n_2}$ and by using the value of $n_2$, we get a meaningful midpoint for the saturation ($K_m$ in conc) at 4 µM. (c) The SP model with individual fits of the secondary rate constant, $k_2k_+$. The free parameter allows for much better agreement with the experimental curves but with a resulting loss of global information. The global parameters were $n_c$ = 1.45, $n_2$ = 2.8, $k_+k_n$ = $10^5$ and the individual $k_+k_2$ parameters for 4, 8, 16 µM were $2.6 \cdot 10^{20}$, $8.2 \cdot 10^{19}$, and $9.2 \cdot 10^{18}$, respectively, which suggests a decrease of the secondary pathway contribution at higher C-36 concentrations. All fits were carried out with the Amylofit online tool (16).

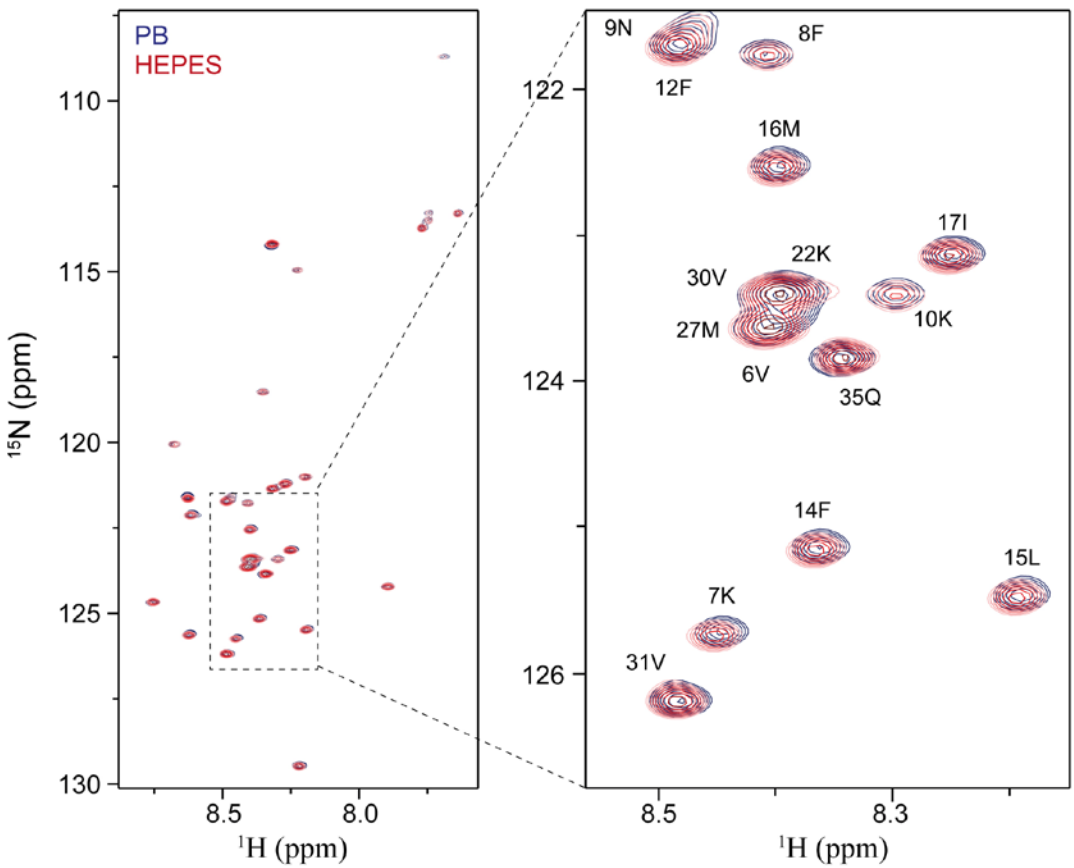


***FIGURE S5 C-36 shows similar chemical shift correlations in PB and HEPES buffer***
Liquid-state NMR $^{1}$H-$^{15}$N-HSQC for C-36 in PB (blue) and HEPES (red) buffer recorded at 5 °C with a peptide concentration of 200 µM. Resonances corresponding to various backbone amides across the C-36 sequence are indicated for the zoomed region.

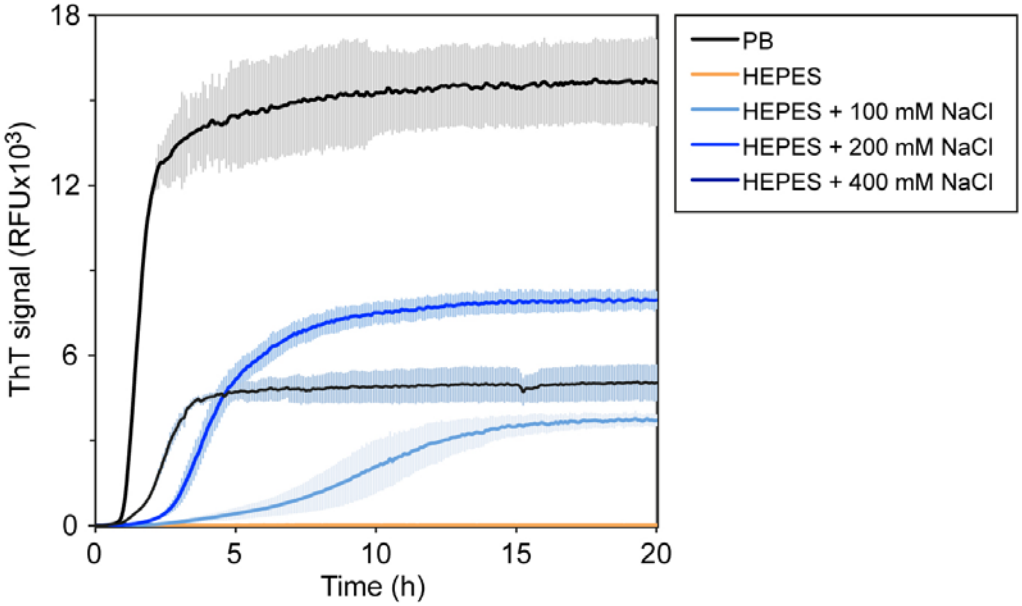


***FIGURE S6 Sodium Chloride potentiates C-36 fibrillation in HEPES buffer***
C-36 reactions (8 µM) were set up in HEPES buffer in PS plates with the indicated amount of NaCl. A set of reactions were set up in PB buffer for comparison. Error bars represent the triplicate point standard deviation.

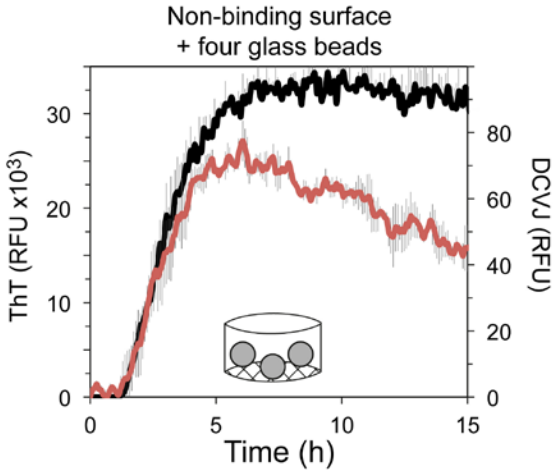


***FIGURE S7 DCVJ signal follows the ThT trace in the presence of glass beads***
ThT and DCVJ fluorescence was measured for 16 µM C-36 fibrillation reactions in NBS plates in the presence or absence of four silica glass beads (ø = 1 mm). The DCVJ signal (red) was similar to the ThT signal (black), ruling out pre-ThT hydrophobic species. Grey error bars indicate the triplicate standard deviation for each point.

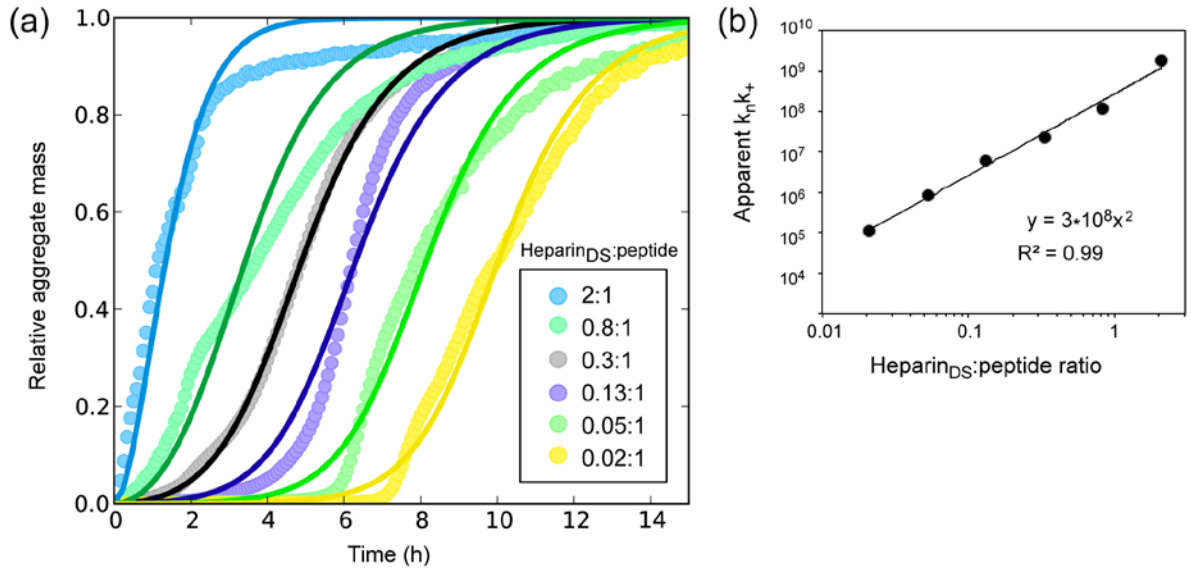


***FIGURE S8 Heparin stimulates C-36 fibrillation by enhancing primary nucleation.***

(a) The major features of the heparin-stimulated C-36 fibrillation in NBS for heparin$_{DS}$:peptide ratios from 0.02 to 0.20 could be captured by the SP model. Nucleus sizes were set to the values found for the global SP fit to C-36 in NBS, which were $n_c$ = 1.85 and $n_2$ = 1.9. The secondary nucleation rate constant was globally fitted to 3.8E-8 and the apparent primary nucleation rate was fitted to each curve individually. (b) The primary nucleation rate constant appeared as a function of the heparin$_{DS}$:peptide ratio squared, illustrating a clear stimulation of this nucleation constant by heparin. If we consider the generation of new aggregates by both homogenous and heparin-accelerated heterogeneous primary nucleation, we get an expression as follows: $\frac{dP}{dt} = k_n {m_0}^{n_c} + k_H {m_0}^{n_c} H^{n_H} = k_n(k_H + H^{n_H}) \cdot {m_0}^{n_c}$ , where H denotes heparin. Under the assumption that heparin contributes with this type concentration-dependent rate enhancement, we can consider the individual fit values of the primary nucleation rate constant in the SP model as apparent rate constants, $k_{app} = k_n(k_H + H^{n_H})$. From this expression, we find the expected power-law scaling behavior of $k_{app}$ as a function of H with a reaction coefficient of $n_H$, which was determined to be 2.0 for heparin's stimulation of C-36 fibrillation.

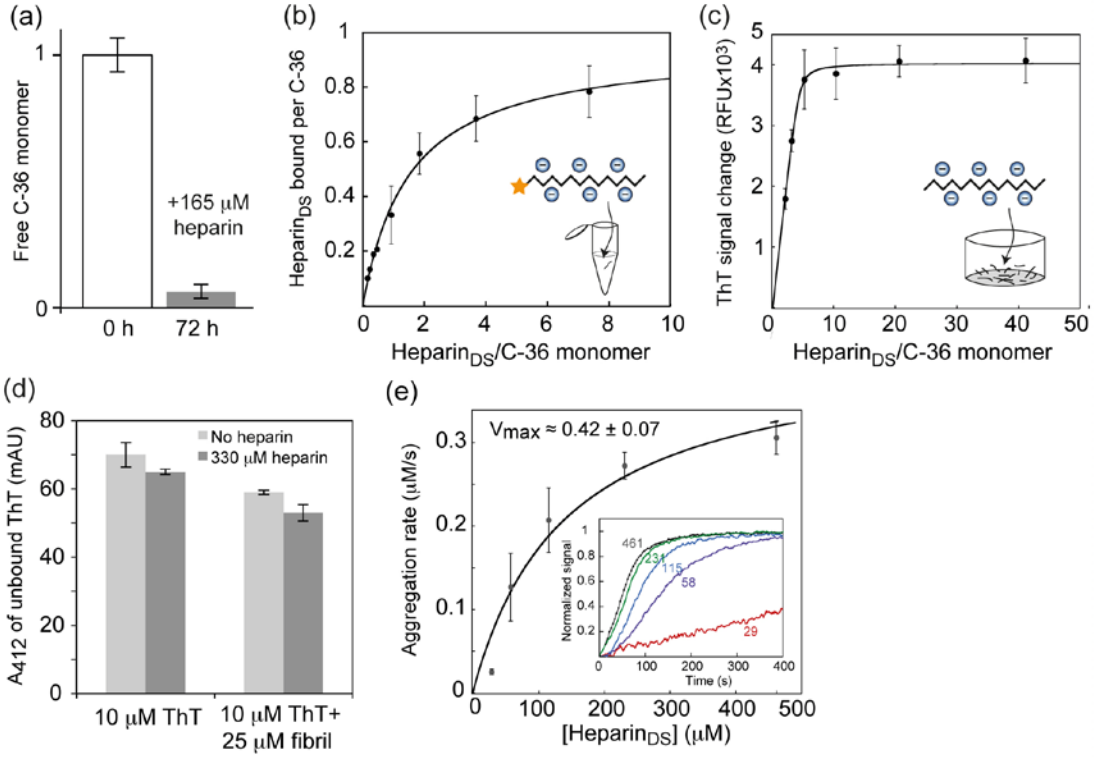


***FIGURE S9 Heparin associates with C-36 aggregates and alters ThT fluorescence***

(a) Residual monomer was quantified by gel filtration before and after incubation with heparin for 72 h. (b) FITC-heparin binding per C-36 monomer ($R_H$), as a function of the heparin$_{DS}$:peptide ratio ($R_{H0}$). The binding was quantified by the residual FITC-heparin amount left in the supernatant after co-incubation with fibrils for 1 h. Fitting was done with the equation $R_H = R_{H0}*R_{max}/(K_d+R_{H0})$, resulting in an $R_{max}$ of 0.96 ± 0.03 (c) ThT fluorescence change of pre-formed C-36 fibrils as a function of the added heparin amount, expressed as the heparin$_{DS}$_peptide ratio. Larger variations are seen due to variations in the actual endpoint ThT level of the in-plate pre-formed C-36 fibrils. (d) Quantification of the unbound ThT by absorbance at 405 nm in the presence of heparin and C-36 fibrils. Heparin does not diminish the ThT binding to fibrils. (e) Time-course profiles for the change in β-sheet content at 222 nm were recorded for heparin$_{DS}$:peptide ratios ranging from 1.2:1 to 18.5:1 (29-461 μM of heparin$_{DS}$). Extracted C-36 aggregation rates were plotted as a function of heparin concentration. Insert shows normalized CD signal change for indicated heparin$_{DS}$ concentrations.

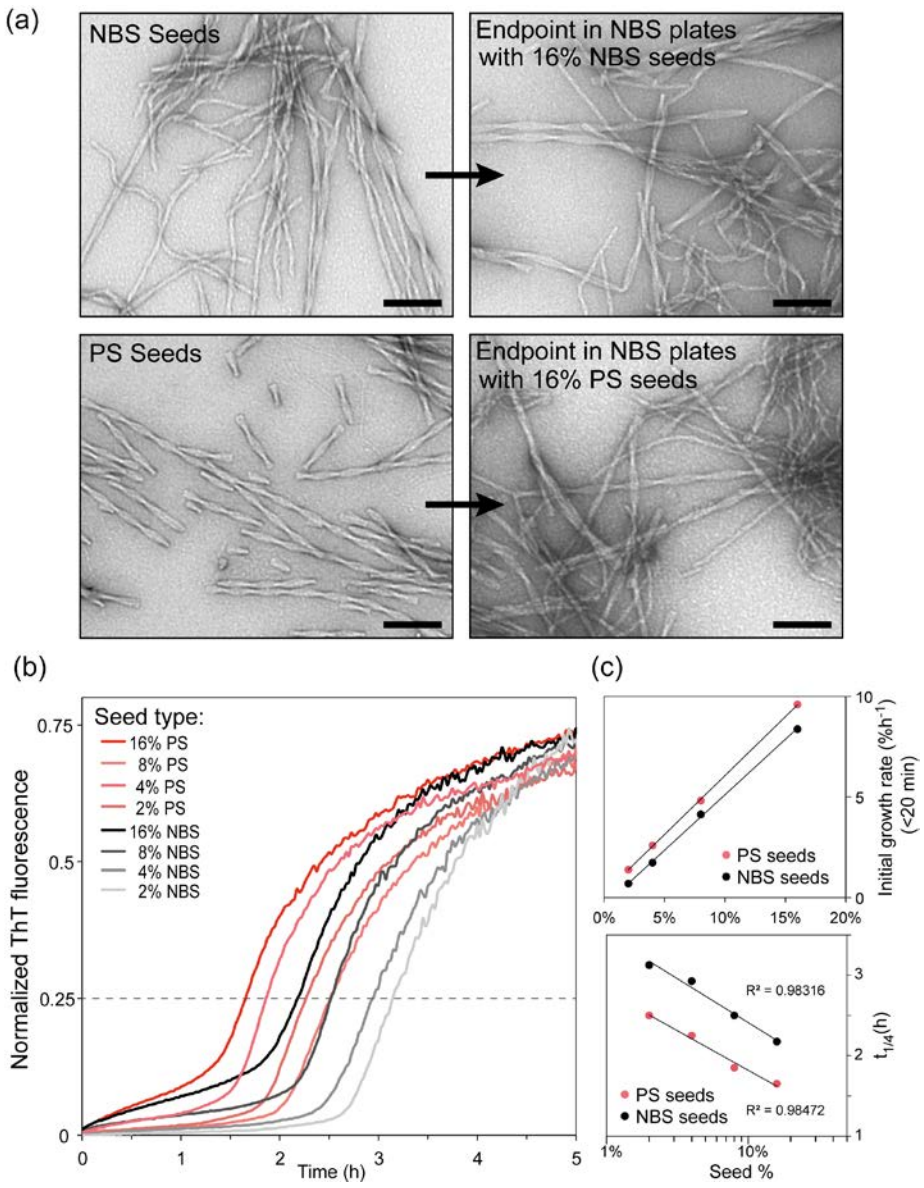


***FIGURE S10 Surface-generated twisted ribbon seeds accelerate bulk nucleation***

(a) TEM images of the NBS and PS fibril populations used for seeds (left) and the endpoint species observed after fibrillation in NBS plates in the presence of 16% of either seed type (right). (b) Triplicate average ThT traces after the addition of the indicated seed amount to 8 μM C-36 and subtraction of the initial ThT value. (c) For both NBS and PS seeds, the initial fibril growth rates (<25 min) correlated linearly with the seed amount (top) and the addition of seeds caused a semi-log scaling behavior of $t_{1/4}$ as a function of seed concentration (bottom) (2, 17). The dashed line in (b) represents the 25% value of the normalized ThT traces from which $t_{1/4}$ is derived. We used $t_{1/4}$ in place of $t_{1/2}$ that did not accurately reflect the fibrillation growth phase in this case. PS seeds stimulated secondary pathways (smaller $t_{1/4}$ values) slightly better than NBS seeds. This may indicate that the ribbon-twist morphology had a higher secondary nucleation potential than alternate NBS morphologies, in line with observed differences in co-existing polymorphs' seeding ability for other amyloid systems such as Aβ (18, 19).

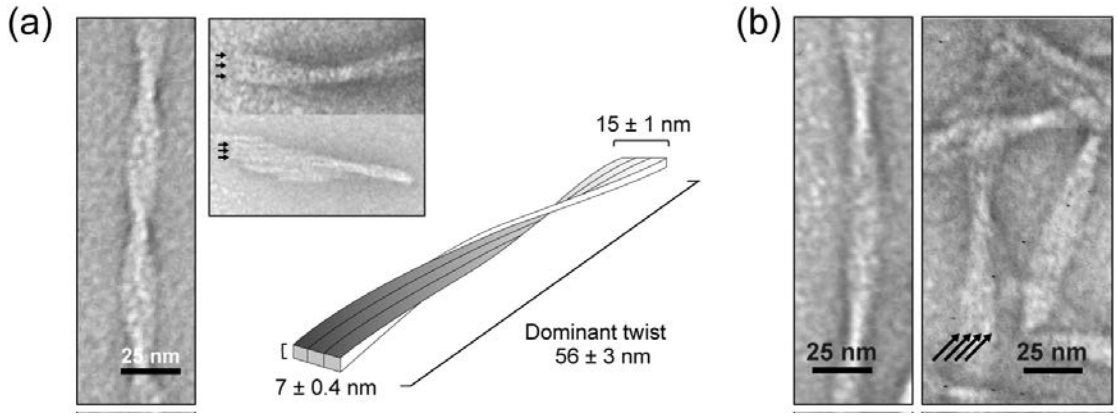


***FIGURE S11 Ribbon morphology details for PS and glass-induced C-36 fibrils***

(a) The ribbon twist morphology of PS fibrils consisted of three twisting laterally associated protofibrils (indicated by arrows) with a ribbon width of 15 nm. The lateral association is also illustrated by a sheet of fibrils occurring under high agitation. Graphic shows a model fibril with measured fibril dimensions (n = 50) (b) Glass-induced fibrils had a larger width of 16 nm, a twist periodicity of 89 nm, and consisted of four laterally associated protofibrils (indicated by arrows).

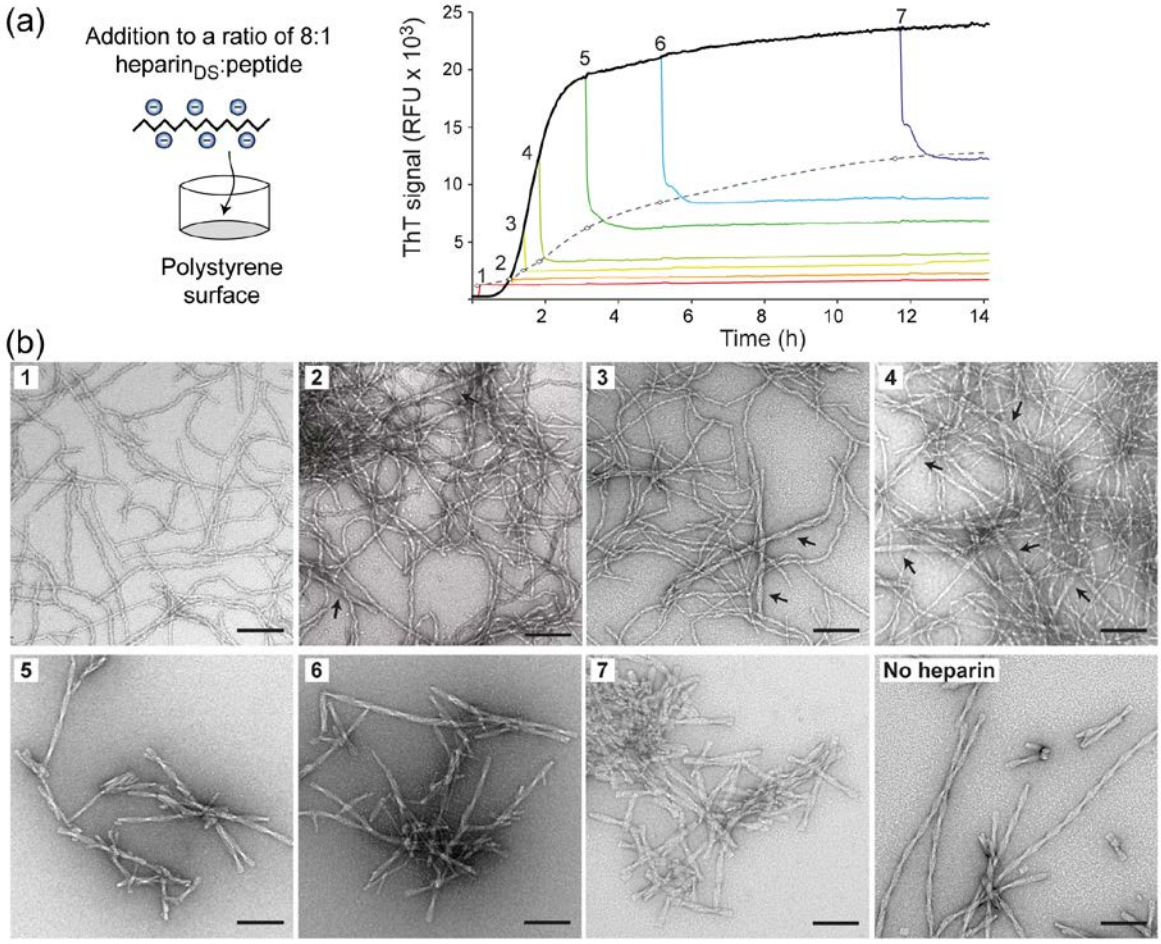


***FIGURE S12 Heparin remodels monomeric C-36 and binds existing fibrils***

(a) ThT traces after indicated additions of heparin to the ongoing fibrillation reactions of 10 µM C-36 in PS plates. Heparin modulates the ThT fluorescence level for all additions but the effect was diminished at later time points with higher ThT levels. The plateau ThT level reached for each heparin addition is indicated by circles which are connected by a stapled line to illustrate the saturation behavior (b) Morphology of the amyloid fibrils at the end of the fibrillation reaction (20 h). Arrows indicate the presence of ribbon twist fibrils for images 2-4. The amount of ribbon twist fibrils correlated with the ThT level increase before heparin addition. No effect of heparin on fibril morphology is seen when heparin is added to C-36 reactions that approached the ThT plateau (images 5-7).

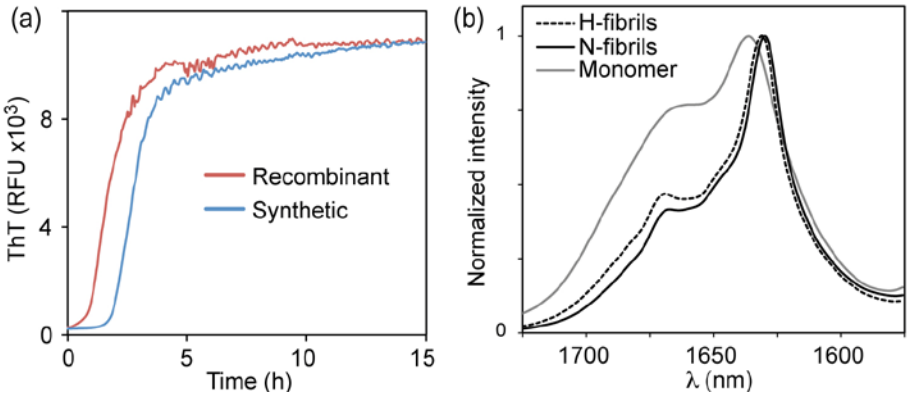


***FIGURE S13 Fibrillation of recombinant and synthetic C-36 and comparison of heparin- and non-heparin fibrils by FTIR***

(a) ThT traces of 8 µM recombinant and synthetic C-36 suggest similar fibrillation behavior. (b) FT-IR spectra in the amide I region from 1600-1700 nm of heparin-induced and non-heparin amyloid fibrils (H- and N-fibrils) was similar with a peak centered at 1630 nm, which is in the classic amyloid β-sheet H-bonded carbonyl stretching frequency range (20). The monomeric C-36 had a different spectral profile and displayed partial β-sheet characteristics in this water-removed dry state.

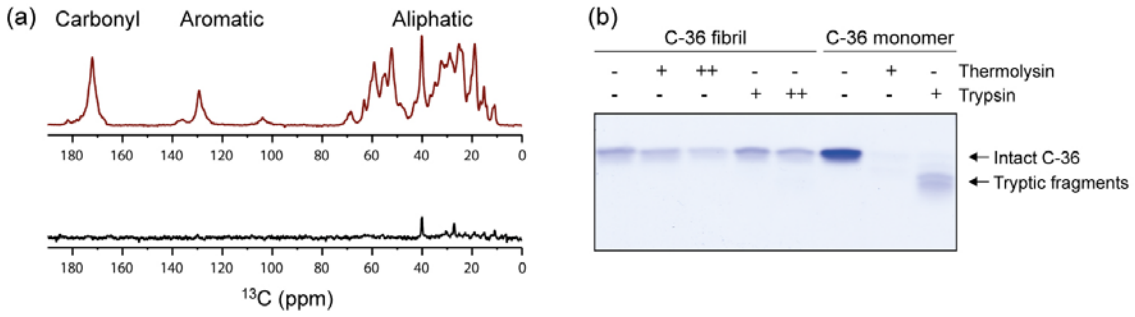


***FIGURE S14 ssNMR 13C-signals and proteolytic protection support full fibril incorporation of the C-36 sequence***

(a) $^{13}$C-signals from the solid region of C-36 fibrils measured by a dipolar-based cross-polarization ssNMR experiment (top) and $^{13}$C-signals from the mobile region of C-36 fibrils measured by a J-coupling-based INEPT-like ssNMR experiment (bottom). The lack of any significant signals above noise in the J-coupling-based experiment suggested incorporation of all the C-36 residues into the solid-phase fibril arrangement. (b) 3 µg of monomeric and fully fibrillated C-36 were subjected to proteolysis by thermolysin or trypsin for 2 h. C-36 contains three internal tryptic sites, K7, K22, and K29. While the monomer was completely digested within this time frame, the fibrillar form largely resisted proteolysis, suggesting a lack of proteolytically accessible flexible loops and full incorporation of the entire peptide sequence into an amyloid structure.

## SUPPORTING REFERENCES


1. Cohen, S. I., M. Vendruscolo, C. M. Dobson, and T. J. Knowles. 2013. The Kinetics and Mechanisms of Amyloid Formation. In Amyloid Fibrils and Prefibrillar Aggregates: Molecular and Biological Properties. D. E. Otzen, editor. Wiley-VCH Verlag GmbH & Co. KGaA.
2. Knowles, T. P. J., C. A. Waudby, G. L. Devlin, S. I. Cohen, A. Aguzzi, M. Vendruscolo, E. M. Terentjev, M. E. Welland, and C. M. Dobson. 2009. An analytical solution to the kinetics of breakable filament assembly. Science 326:1533-1537.
3. Cohen, S. I., S. Linse, L. M. Luheshi, E. Hellstrand, D. A. White, L. Rajah, D. E. Otzen, M. Vendruscolo, C. M. Dobson, and T. P. Knowles. 2013. Proliferation of amyloid-beta42 aggregates occurs through a secondary nucleation mechanism. Proc Natl Acad Sci U S A 110:9758-9763.
4. Cohen, S. I. A., M. Vendruscolo, C. M. Dobson, and T. P. J. Knowles. 2012. From macroscopic measurements to microscopic mechanisms of protein aggregation. J Mol Biol 421:160-171.
5. Cohen, S. I. A., M. Vendruscolo, M. E. Welland, C. M. Dobson, E. M. Terentjev, and T. P. J. Knowles. 2011. Nucleated polymerization with secondary pathways. I. Time evolution of the principal moments. J Chem Phys 135:065105.
6. Manning, G. S. 2008. Approximate Solutions to Some Problems in Polyelectrolyte Theory Involving Nonuniform Charge Distributions. Macromolecules 41:6217-6227.
7. Manning, G. S. 1969. Limiting Laws and Counterion Condensation in Polyelectrolyte Solutions I. Colligative Properties. The Journal of Chemical Physics 51:924-933.
8. Diakun, G. P., H. E. Edwards, D. J. Wedlock, J. C. Allen, and G. O. Phillips. 1978. The Relationship between Counterion Activity Coefficients and the Anticoagulant Activity of Heparin. Macromolecules 11:1110-1114.
9. Rabenstein, D. L., J. M. Robert, and J. Peng. 1995. Multinuclear magnetic resonance studies of the interaction of inorganic cations with heparin. Carbohydrate research 278:239-256.
10. Beirne, J., H. Truchan, and L. Rao. 2011. Development and qualification of a size exclusion chromatography coupled with multiangle light scattering method for molecular weight determination of unfractionated heparin. Anal Bioanal Chem 399:717-725.

11. Oktaviani, N. A., M. W. Risor, Y. H. Lee, R. P. Megens, D. H. de Jong, R. Otten, R. M. Scheek, J. J. Enghild, N. C. Nielsen, T. Ikegami, and F. A. Mulder. 2015. Optimized co-solute paramagnetic relaxation enhancement for the rapid NMR analysis of a highly fibrillogenic peptide. J Biomol NMR 62:129-142.
12. Hu, K.-N., R. P. McGlinchey, R. B. Wickner, and R. Tycko. 2011. Segmental polymorphism in a functional amyloid. Biophys J 101:2242-2250.
13. Kryndushkin, D. S., R. B. Wickner, and R. Tycko. 2011. The core of Ure2p prion fibrils is formed by the N-terminal segment in a parallel cross-$\beta$ structure: evidence from solid-state NMR. J Mol Biol 409:263-277.
14. Fung, B. M., A. K. Khitrin, and K. Ermolaev. 2000. An improved broadband decoupling sequence for liquid crystals and solids. J Magn Reson 142:97-101.
15. Meisl, G., X. Yang, E. Hellstrand, B. Frohm, J. B. Kirkegaard, S. I. A. Cohen, C. M. Dobson, S. Linse, and T. P. J. Knowles. 2014. Differences in nucleation behavior underlie the contrasting aggregation kinetics of the A$\beta$40 and A$\beta$42 peptides. Proc Natl Acad Sci USA 111:9384-9389.
16. Meisl, G., J. B. Kirkegaard, P. Arosio, T. C. Michaels, M. Vendruscolo, C. M. Dobson, S. Linse, and T. P. Knowles. 2016. Molecular mechanisms of protein aggregation from global fitting of kinetic models. Nature protocols 11:252-272.
17. Lorenzen, N., S. I. Cohen, S. B. Nielsen, T. W. Herling, G. Christiansen, C. M. Dobson, T. P. Knowles, and D. Otzen. 2012. Role of elongation and secondary pathways in S6 amyloid fibril growth. Biophysical journal 102:2167-2175.
18. Paravastu, A. K., A. T. Petkova, and R. Tycko. 2006. Polymorphic fibril formation by residues 10-40 of the Alzheimer's beta-amyloid peptide. Biophys J 90:4618-4629.
19. Petkova, A. T., R. D. Leapman, Z. Guo, W.-M. Yau, M. P. Mattson, and R. Tycko. 2005. Self-propagating, molecular-level polymorphism in Alzheimer's beta-amyloid fibrils. Science 307:262-265.
20. Zandomeneghi, G., M. R. Krebs, M. G. McCammon, and M. Fandrich. 2004. FTIR reveals structural differences between native beta-sheet proteins and amyloid fibrils. Protein Sci 13:3314-3321.